Engineering the Performance of 2D Transition Metal Dichalcogenide Nanotransistors through Quantum Transport Simulations

by

Manasa Kaniselvan

A thesis
presented to the University of Waterloo
in fulfillment of the
thesis requirement for the degree of
Master of Applied Science
in
Electrical and Computer Engineering,
(Nanotechnology)

Waterloo, Ontario, Canada, 2021

Author's Declaration

This thesis consists of material all of which I authored or co-authored: see Statement of Contributions included in the thesis. This is a true copy of the thesis, including any required final revisions, as accepted by my examiners.

I understand that my thesis may be made electronically available to the public.

Abstract

Two-dimensional (2D) transition metal dichalcogenides (TMDs) are a class of stable, atomically-thin monolayer materials with unique mechanical and electronic properties, leading to several proposed applications in electronics and optoelectronics. This thesis presents two studies in which ab-initio numerical simulations based on the Non-Equilibrium Green's Function method were used to model the performance of these materials in photodetector and tunnel field-effect transistor (TFET) devices.

The first study presents the design and operation of a MoS_2 photodetector, in which the superior electrostatic control provided by the atomically thin device channel allows for the design of a unique, 'grounded-gate' device where the source and gate controls are permanently connected. This is done in order to introduce a rectification effect which suppresses the dark current to increase the device's sensitivity. Numerical simulations using an effective-mass approach to model the electronic states of the channel, along with an analytical model for photoconductivity, were used to explain the device operation and reproduce trends in the experimental data. The resulting experimentally-fabricated device shows a high sensitivity of 1.01 A/W and detectivity above 6 $\times$ 10^{10} Jones. Using the simulations, it is then suggested that engineering the gate metal work function can lead to an additional increase in sensitivity by three orders of magnitude.

The second study presents the numerical design and performance analysis of a strained $PtSe_2$ TFET which can deliver high ON-currents. Though they can provide the high level of electrostatic control required to achieve steep-switching, monolayer TMD TFETs typically do not have high ON-currents due to high bandgaps, high effective masses, and/or lack a direct path to facilitate band-to-band tunneling. However, these materials are highly flexible, and mechanical strain is able to modulate the electronic bandstructure of $PtSe_2$ to an extent where it can show ideal properties for use in TFETs. Under biaxial tensile strain, its bandgap and effective mass can be reduced significantly, and a direct path for tunneling emerges. Simulated results show that a double-gated $PtSe_2$ TFET device strained to +5% can drive an ON-current above 100 μA/μm while maintaining an OFF-current below 1×10^{-7} μA/μm and a sub-thermionic subthreshold swing. This improvement comes at a reasonable cost of OFF-current degradation and minimal effect on the switching characteristics down to 10 nm channel lengths. These results present the flexibility of monolayer TMDs as a powerful tuning parameter towards their use in tunneling devices.

Acknowledgements

I would like to first acknowledge my advisor, Prof. Youngki Yoon, for his outstanding supervision over the past year. His patient explanations regarding technical details relevant to my work were invaluable in helping me better understand semiconductors and device physics. This directly translated to both my progress in research and my increasing fascination with this field.

I would also like to thank my group mates Richard and Demin for answering all my questions, of which I had many. Richard's mentorship and guidance since I started my MASc is highly appreciated, and it was really great to work with him on my first two projects. Thanks also to Rob, Hyunjae, and Yiju for making the office a fun place to be!

I am grateful to my parents for the high level of importance they've placed on my education since I was young, which allowed me to have goals as lofty as I could make them.

And thank you so much to Jérémie for being with me every step of the way.

Table of Contents

List of Figures

List of Abbreviations

BP Black Phosphorus

BZ Brillouin Zone

DFT Density Functional Theory

FET Field Effect Transistor

GGA Generalized Gradient Approximation

LDA Local Density Approximation

MLWF Maximally Localized Wannier Function

MoS_2 Molybdenum Disulfide

$MoSe_2$ Molybdenum Diselenide

NEGF Non-Equilibrium Greens Function

PAW Projector Augmented Wave

$PtSe_2$ Platinum Diselenide

SS Subthreshold Swing

TFET Tunnel Field Effect Transistor

TMD Transition Metal Dichalcogenide

WS_2 Tungsten Disulfide

WSe_2 Tungsten Diselenide

1

Introduction

As we approach the physical and material limitations of bulk silicon for (opto)electronic devices, we require new electronic materials that can show high-performance, low-power consumption, and/or strong light-matter interactions. The class of two-dimensional (2D) materials present promising contenders to satisfy these requirements. In these materials, covalent bonds occur within an atomically thin layer, and interlayer interactions are limited to weaker Van der Waals forces. As a result of this, they can be easily exfoliated into stable, individual monolayers. Although the most famous example is graphene [1], since its discovery in 2004 multiple other metallic and semiconducting 2D materials made with different atomic species have been grown experimentally. Theoretical studies have identified over one thousand stable monolayer materials which could potentially be grown or exfoliated from their bulk counterparts [2]. Fig.1.1 illustrates some of the configurations which these monolayers come in, including planar, buckled, and sandwich structures.

Applications of these materials range from transistors to optoelectronics to biosensing (Fig. 1.2), where their unique electronic and material properties can be harnessed to design devices. For transistors, they offer the possibility of scaling the channel down to an atomic thickness. Fig.1.3 presents a schematic of the traditional bulk planar MOSFET, as well as several modern device architectures which display better electrostatic control. The Ultra-Thin Body Silicon on Insulator (UTB-SOI) FET and the FinFET present much thinner channels, and the resulting superior gate-control leads to lower leakage currents in the OFF-state and sharper subthreshold swings. However, these methods of architectural optimization run into problems when scaled down to the atomic level as they encounter fundamental limitations of the channel material itself; quantum confinement, edge roughness, and short-channel effects begin to play a large part in the quality of device operation.

In 2D FETs, the channel thickness can be reduced to the order of 0.5 nm (compared to UTB-SOI FETs and FinFETS where this is still in the tens of nanometers) while avoiding many of these

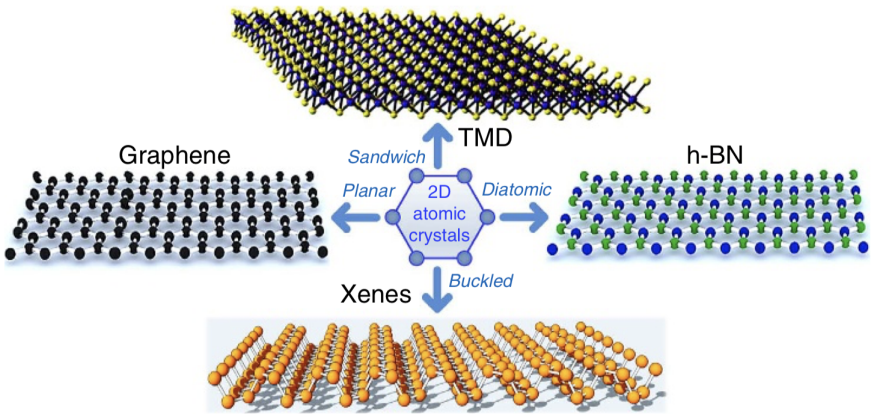

Figure 1.1: Schematic illustrations of different configurations of 2D monolayer materials, including monoatomic planar sheets such as graphene, chalcogen-transition metal-chalcogen sandwiches such as molybdenum disulfide (MoS_2), diatomic planar sheets like hexagonal boron nitride (h-BN), and buckled structures such as black phosphorus. Adapted from Ref [3]

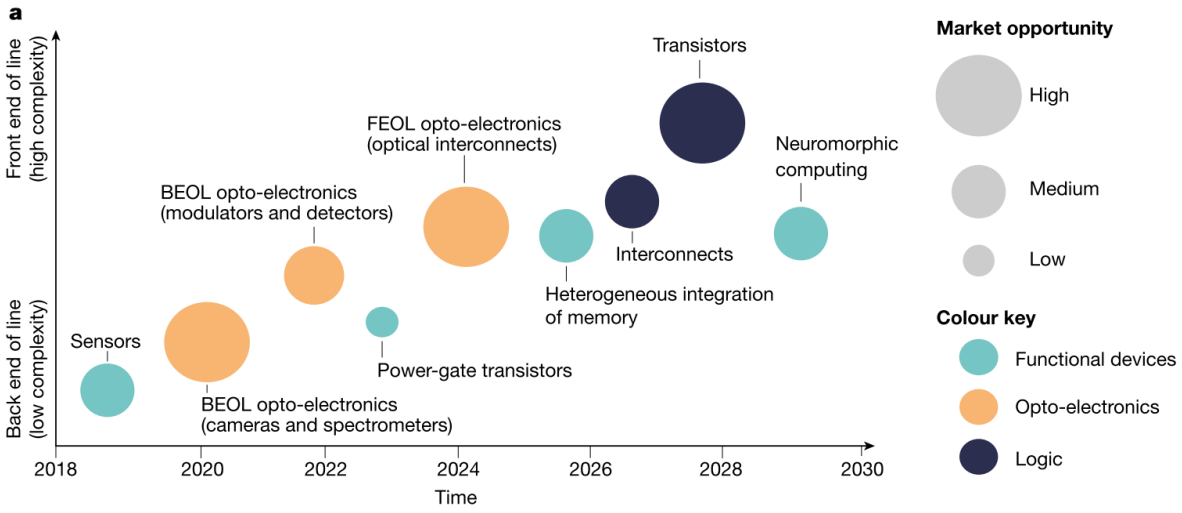

Figure 1.2: Potential applications for 2D layered semiconductors, in Back End-of-Line (BEOL) and Front End-of-line (FEOL) electronics. Market opportunity and complexity are indicated by the size and location of each application. Adapted from Ref [4].

issues. The lack of atomic bonds in the out-of-plane direction leads to a reduced extent of interface scattering, allowing several 2D materials to show far higher carrier mobilities when compared to

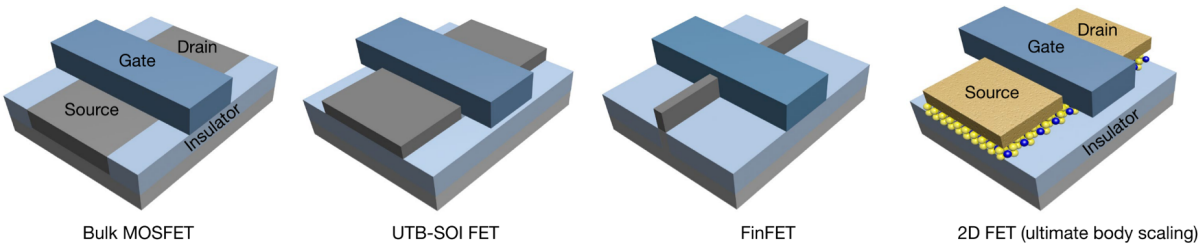

Figure 1.3: Schematics of several transistor architectures, include the conventional bulk Metal-Oxide-Semiconductor (MOS) FET, Ultra-Thin Body Silion-on-Insulator (UTB-SOI) FET, vertical Fin FET, and a 2D FET in which the channel is a monolayer 2D material. Adapted from Ref [5].

bulk-counterparts scaled down to a similar thickness [5]. The thinness of the channel leads to a sharper variation of electrostatic potential at the source-channel and channel-drain interfaces, helping to mitigate certain short-channel effects [4, 5]. 2D electronics also offer the possibility of new architectures which are not achievable with conventional bulk semiconductors. Several new sharp-switching devices, such as the Tunnel Field-Effect Transistor (TFET), require an incredibly high level of electrostatic control in order to achieve their theoretical potential in operation, and narrow-gap 2D materials have therefore been extensively investigated for such devices [6, 7, 8, 9]. The lack of interlayer bonds also allows for 2D monolayers to be vertically stacked without concern for lattice-matching [5], which leads to the possibility of new, vertically-integrated '3D' chip designs [10].

Another application in which 2D TMD materials have displayed potential is in the development of photodetectors. Photodetectors, or devices which convert an optical input into a current signal, are present in a variety of optical sensing, imaging, and communication systems. They typically consist of a semiconducting material in which photogenerated excitons are separated by an electric field. The performance of a photodetector is then dependent on the intrinsic ability of a material to absorb light to form excitons. To this end, photodetectors made with direct-gap 2D transition-metal-dichalcogenides (TMDs) can show incredibly high optical absorption; a single monolayer of MoS_2 can absorb the equivalent of 50 nm of bulk silicon [11]. Within the visible range, 2H-MoS_2 has the highest absorption of near 27% (Fig.1.4a), and it is consequently the most popular TMD used for optoelectronic applications.

Photodetectors are typically characterized by their responsivity (variation of output signal commensurate with the amount of incident light), detectivity (sensitivity to low input signals) and response time (speed of output variation in response to variation in the input signal). Fig.1.4b and c display these figures of merit as previously reported in literature for several 2D TMD materials such as black phosphorus (BP), MoS_2, WS_2, and WSe_2. For comparison, those of bulk

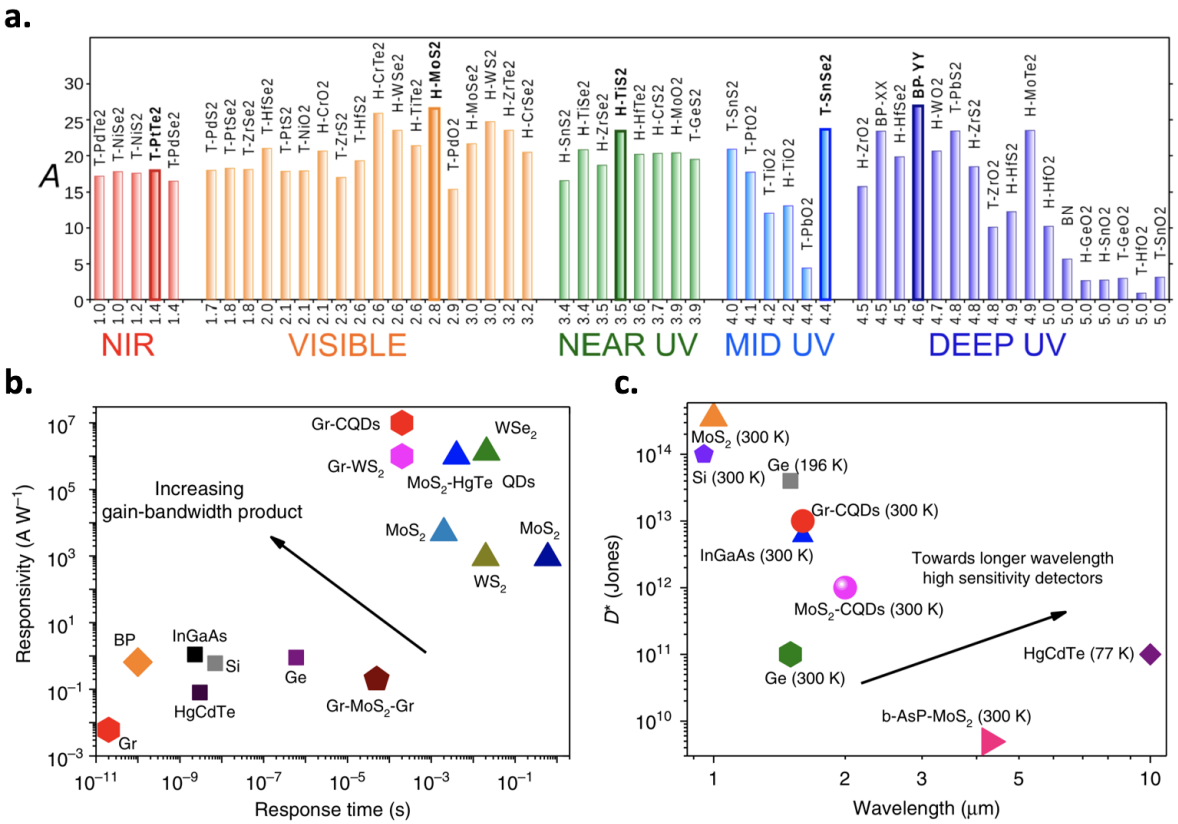

Figure 1.4: a. Absorption of several 2D monolayers (in %) at energies 1 eV $< \hbar\omega <$ 5 eV, from the near infrared (NIR) to deep UV, adapted from Ref [12]. Responsivity (b.) and Detectivity (c.) values from literature for several 2D materials and bulk materials commonly used in photodetectors, as well as graphene/colloidal quantum dots (Gr-CQDs), and quantum dots (QDs). Adapted from Ref [13].

materials such as silicon, indium gallium arsenide, and germanium are also pictured. Compared to the bulk material devices, those made with TMDs typically show higher responsivity at the cost of a reduction in response time. MoS_2 in particular shows both outstanding responsivity and detectivity values, which has been seen in many previous reports [14, 15, 16].

The atomically thin nature and lack of interlayer covalent bonds also allows these materials to show high levels of flexibility and mechanical robustness [3, 17], which introduces numerous straintronic applications that conventional rigid semiconductors are too brittle for. In particular, monolayer MoS_2 can withstand high tensile strains of up to 11% before rupture [18]. Successfully depositing these materials onto flexible substrates could result in the development of highly robust

wearable electronics. In addition, mechanical strain can be used as a tuning knob for electronic properties; the material bandgap, effective mass, and carrier mobility all vary as the orbital structure changes with applied strain [19].

This thesis outlines two projects in which ab-initio quantum transport frameworks have been used to design and evaluate 2D material nanoelectronic devices. These designs exploit their unique material properties (eg, atomic thinness, strong light-matter interactions, and flexibility) which allow them to show superior performance to conventional bulk semiconductors in the ultimately-scaled device regime. The organization is as follows: Chapter 2 provides an overview of the numerical methods used to simulate the performance of TMD-based devices in this thesis. These methods are then used in two seperate studies, which are detailed in Chapters 3 and 4. Finally, we conclude with a discussion of potential future work to extend these studies.

2

Simulation Methods

In the absence of mature fabrication methods for new materials, numerical simulations have been an invaluable tool to evaluate their potential prior to designing devices. For the field of 2D-material electronics in particular, much of the work has been computational, from materials discovery [2] to device performance assessment [20]. The methods used to simulate these devices have ranged from analytical models, to semi-classical drift diffusion, to the most accurate full-band quantum-transport simulations. Figure 2.1 shows some of these methods in an order of accuracy (and consequently, computational demand) for calculating the electronic properties of the 2D materials used in device channels (top row), and simulating carrier transport through devices made with them (bottom row).

The dimensions of the devices simulated in this thesis are well within the regime where quantum effects such as tunneling begin to occur, so simple analytical models are inaccurate. However, these short channel lengths are on the same order of magnitude as the diffusion lengths of individual carriers, and transport is mostly ballistic. To achieve a compromise between an accurate reproduction of quantum mechanical effects and manageable computational burden, in this thesis the Non-Equilibrium Green's Function (NEGF) based transport model is employed under a ballistic transport approximation.

The electronic states of the channel are describes with two different approaches; the phototransistor channel in Chapter 3 is modelled with a simple analytical effective-mass model which is sufficient to describe the dark current, and the TFET in Chapter 4 is simulated using a Hamiltonian made with Maximally Localized Wannier Functions (MLWF) which can accurately capture the variation in band position when strain is applied. In the latter approach, electronic bandstructures are first calculated using Density Functional Theory (DFT), then a basis set of Maximally Localized Wannier Function (MLWF) orbitals is selected which best fits this DFT calculation, and finally this set of MWLFs is converted into a Hamiltonian matrix of interaction parameters which can be used to represent the material in device simulations.

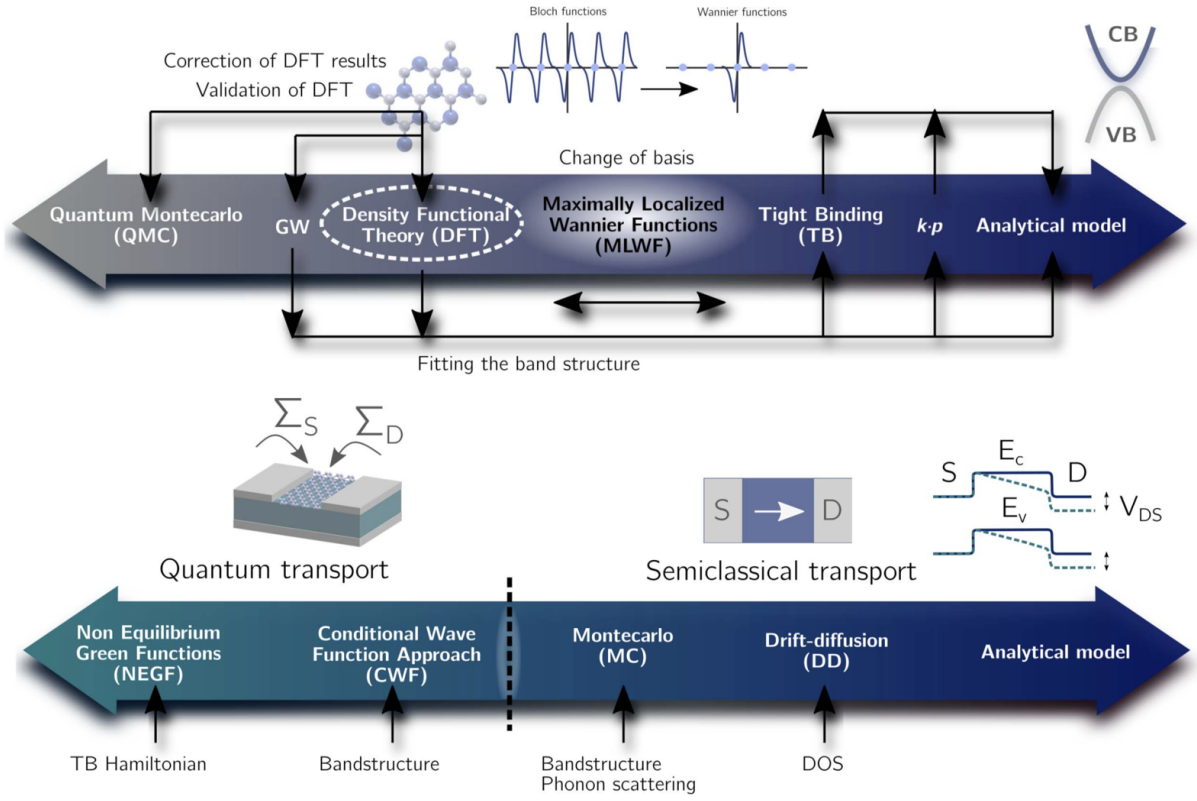

Figure 2.1: Modelling approaches used for the calculation of material electronic properties (top row), and device transport (bottom row), pictured from most complex (left) to the simplest analytical model (right). Adapted from Ref [21].

This chapter briefly introduces some of the methods used in the following studies. Although the entire formalism of DFT is outside the scope of this thesis, I summarize it briefly in section 2.1 and then focus on the methods used to extract and post-process the relevant parameters calculated with the Quantum Espresso DFT code. Section 2.2 then reviews how these quantities are used in the NEGF transport framework.

2.1 Electronic Structure Calculations for 2D TMDs

2.1.1 Density Functional Theory

The Density Functional Theory framework for electronic structure calculations is based on the idea that all physical properties of a system can be calculated using knowledge of the electron density $n(\mathbf{r})$[1]. The core process requires iteratively solving for the wavefunctions, which are found as the eigenstates of the Hamiltonian:

$$H[n(\mathbf{r})]\psi_j(\mathbf{r}) = \varepsilon_j\psi_j(\mathbf{r}) \tag{2.1}$$

and the electron density, which is the sum of the squared wavefunction over all space:

$$n(\mathbf{r}) = \sum_j f_j|\psi(\mathbf{r})|^2 \tag{2.2}$$

where $H[n]$ is the Hamiltonian (a non-trivial function of the electron density n($\mathbf{r}$)), $\psi_j(\mathbf{r})$ are atomic orbitals, ε_j are the corresponding eigenvalues, and f_j is the occupation factor of state j. I use the notation of 'f(x)' to define a function of x (takes a scalar x and outputs a scalar) and 'F[x]' to define a functional of x (takes a function x and outputs a scalar). In this case, there is a unique energy for every unique electron density (defined for values of $\mathbf{r}$), so the Hamiltonian is a functional of the density in Eqn.2.1. The density is further constrained by the condition that it must be equal to the total number of electrons N in the system when integrated over all space.

Equations 2.1 and 2.2[2] are solved self-consistently. We first input a unit cell, specifying the identities and locations of all the atoms within it. Then, the corresponding initial atomic orbital information is used to create a 'trial' electron density $n_0(\mathbf{r})$. This $n_0(\mathbf{r})$ is used to form the hamiltonian $H[n(\mathbf{r})]$ in Eqn.2.1, which is then diagonalized to find a set of atomic orbitals $\psi_j(\mathbf{r})$. This set of atomic orbitals is used to recalculate the electron density $n(\mathbf{r})$ in Eqn.2.2. The process above is repeated until the differences in the atomic orbital set and electron density across iterations are both below a prespecified tolerance.

A significant part of the DFT framework is then dedicated to finding an expression for and solving $H[n(\mathbf{r})]$. We know that the form of the one-electron Hamiltonian is:

$$H = \left[\frac{\hbar^2\nabla^2}{2m} + U(\mathbf{r})\right] \tag{2.3}$$

[1] Kato's Theorem [22]

[2] These are the 'Kohn-Sham' equations.

Where m is the electronic mass and $U(\mathbf{r})$ is an external potential. However, this form does not include electron-electron interactions, and so when used for a system of N electrons it represents the 'non-interacting' case which may have a very different density $n(\mathbf{r})$ from the same system with interactions considered. Since all quantities are being derived from $n(\mathbf{r})$, this quantity should ideally be exact in representing the full, interacting system.

To address this, an 'effective potential' $V_s(\mathbf{r})$ is used, defined such that if $V_s(\mathbf{r})$ is used in place of $U(\mathbf{r})$ in Eqn.2.3, the resulting electron density of the non-interacting system will be equal to the density of the corresponding interacting system. The form used for $V_s(\mathbf{r})$ is:

$$V_s(\mathbf{r}) = U(\mathbf{r}) + e^2 \int d^3r \frac{n(\mathbf{r'})}{|\mathbf{r} - \mathbf{r'}|} + V_{xc}(\mathbf{r}, [n(\mathbf{r})]) \tag{2.4}$$

where the first term is the usual external potential, the second term is a Coulomb repulsion, and the third term is an exchange correlation potential - a 'virtual' potential term which forces the density to match that of the interacting system. Both the second and third terms depend on the electron density, which depends on the orbitals, which depend on the Hamiltonian, which depends on this term V_s. This circular dependancy is addressed during the self-consistent procedure to solve Eqns.2.1 and 2.2.

The difficulty has now been shifted to determining a form for $V_{xc}(\mathbf{r}, [n])$, or the 'exchange correlation energy' $E_{xc}[n(\mathbf{r})]$ such that $V_{xc}(\mathbf{r}, [n]) = \delta E_{xc}[n(\mathbf{r})]/\delta n(\mathbf{r})$, which can reproduce the 'real' density of the interacting system. Physically, $E_{xc}[n(\mathbf{r})]$ represents the energy of the remainder of quantum mechanical interactions between electrons which cannot be described with a simple Coulomb potential. The exact value for $E_{xc}[n(\mathbf{r})]$ is not known, but there are two general approximations used to compute it.

- Local Density Approximation (LDA) [23]

$$E_{xc}^{LDA}[n(\mathbf{r})] = \int d^3\mathbf{r} n(\mathbf{r}) e_{xc}^{HEG}(n(\mathbf{r})) \tag{2.5}$$

  Where e_{xc}^{HEG} is the exchange-correlation energy of a homogenous electron gas (HEG) with the same density everywhere. This is a scalar value which can be solved semi-analytically. This form for $E_{xc}[n(\mathbf{r})]$ therefore only depends on the electron density at every point.

- Generalized Gradient Approximation (GGA) [24]

$$E_{xc}^{GGA}[n(\mathbf{r})] = E_{xc}^{LDA}[n(\mathbf{r})] + \int d^3\mathbf{r} e_{xc}^{GGA}(n(\mathbf{r}), \nabla n(\mathbf{r})) \tag{2.6}$$

  Where $e_{xc}^{GGA}(n(\mathbf{r})$ depends on both the electron density and its derivative, and can be found through several approximations [24]. This form of $E_{xc}[n(\mathbf{r})]$ depends on both the electron density and its gradient, and is considered to be more accurate.

Solving Eqns.2.1 and 2.2 also requires a set of basis functions used to define the atomic orbitals $\psi_j(\mathbf{r})$. In theory, this can be any set of orthogonal functions. To reduce the number of self consistent orbitals which need to be solved by Eqns.2.1 and 2.2, the effective potential of the atomic centers and core electrons are usually represented by pre-calculated 'pseudopotentials' assembled into look-up tables for each atomic species. The valence electrons are then expanded in a plane wave basis:

$$\psi_{j,\mathbf{k}}(\mathbf{r}) = \frac{1}{\sqrt{N\Omega_0}} e^{i\mathbf{k}\cdot\mathbf{r}} u_{j,\mathbf{k}}(\mathbf{r}) \tag{2.7}$$

where Ω_0 is the volume of the cell, $\mathbf{k}$ is a wavevector, and $u_{j,\mathbf{k}}(\mathbf{r})$ is a Bloch function with the periodicity of the lattice (the form for the Bloch wavefunction will be derived in the next section):

$$u_{j,\mathbf{k}}(\mathbf{r}) = \sum_{\mathbf{G}} e^{i\mathbf{G}\cdot\mathbf{r}} u_j(\mathbf{k}+\mathbf{G}) \tag{2.8}$$

The reciprocal lattice vector $\mathbf{G}$ can in theory be infinite, but in practice is summed up to a value corresponding to a maximum kinetic energy cutoff:

$$\frac{\hbar^2|\mathbf{k}+\mathbf{G}|^2}{2m} \leqslant E_{cutoff} \tag{2.9}$$

where it acts as an important convergence parameter for the self-consistent calculation. Recommended values of E_{cutoff} are typically provided within the corresponding pseudopotential files.

The full DFT framework is able to use the converged values of the electron density $n(\mathbf{r})$ and energy functional $E[n(\mathbf{r})]$ to compute physically meaningful properties. For example, the binding energy can be determined by the differences between energy functionals for bonded and isolated systems. The full bandstructure of the system can be obtained by diagonalizing the Hamiltonian over a grid of $\mathbf{k}$-points, from which the bandgap and effective masses can be found. And taking the derivative of $E[n(\mathbf{r})]$ with respect to atomic displacements provides information about the net forces acting on atoms, which (in combination with global optimization methods) can be used to 'relax' the atomic positions within the unit cell to their lowest energy configuration.

In this report, I use the open-source Quantum Espresso [25] code to preform DFT calculations in order to extract atomic orbitals and bandstructure information for monolayer 2D materials such as MoS_2. Typically this is done by defining a unit cell containing both the monolayer atoms (in plane) surrounded by a 2-3 nm of free space. This vaccum space ensures that when the unit case is periodically tiled, the monolayer is far enough apart from its periodic image in the 'z' direction that interlayer interactions are negligible.

2.1.2 Maximally Localized Wannier Functions

The wavefunctions solved for by DFT in the previous section have the form of Bloch waves, which are periodic and defined over all space. However, in order to create tight-binding Hamiltonians (which will be detailed in the next section), we require knowledge about the strength of interaction between individual orbitals within a unit cell and between a unit cell and its nearest neighbor cells. For this, the basis of period Bloch functions need to be converted into a set of localized orbitals which can reproduce the same energy eigenstates.

This can be done by taking superpositions of Bloch functions at **k**-points within the first Brillouin Zone (BZ) [26]:

$$w_0(\mathbf{r}) = \frac{V}{(2\pi)^3} \int_{BZ} d\mathbf{k} \psi_{j,\mathbf{k}} \tag{2.10}$$

The resulting w_0 are 'Maximally Localized Wannier Functions' (MLWF) which are centered on the atom within the unit cell which produced orbital ψ_j, and decay exponentially farther from the atomic center. Adding an additional phase factor within the integral has the effect of shifting this MLWF around in space, where it can be placed on the corresponding atom in another unit cell. If **R** is a real-space translation vector, then the following is a wannier function translated to the atomic center at j:

$$|\mathbf{R}j\rangle = \frac{V}{(2\pi)^3} \int_{BZ} d\mathbf{k} e^{-i\mathbf{k}\cdot\mathbf{R}} |\psi_{j,\mathbf{k}}\rangle \tag{2.11}$$

These MLWFs are not eigenstates of the Hamiltonian, but can be used to produce the same set of energy eigenvalues. In this thesis, I transform the delocalized Bloch wavefunctions used in DFT to a localized MLWF basis using the Wannier90 code [27], and extract effective interactions between them to construct a tight-binding Hamiltonian.

2.1.3 The Tight Binding Approximation

To calculate the electronic states available in a periodic crystal, we use the fact that the electron density must be reproduced when the crystal is shifted by the lattice constant 'a'. For example, in a 1D lattice:

$$\rho(x) = \rho(x+a) = \rho(x+2a) = \rho(x+3a)\ldots \tag{2.12}$$

where $\rho(x)$ is the electron density at position x along the lattice, which can be written as the square of the wavefunction:

$$\rho(x) = \Psi(x)^* \Psi(x) \tag{2.13}$$

For equation 2.12 to be satisfied, the periodicity of the wavefunction $\Psi(x)$ should follow:

$$\begin{aligned} \Psi(x+a) &= \mu \Psi(x) \\ \Psi(x+2a) &= \mu^2 \Psi(x) \\ &\dots \\ \Psi(x+na) &= \mu^n \Psi(x) \end{aligned} \tag{2.14}$$

where μ is a constant such that $\mu^* \mu = 1$, so that the periodicity of the wavefunction is equal to the periodicity of the lattice. To satisfy this condition, μ must be of the form:

$$\mu = e^{ika} \tag{2.15}$$

where 'k' has units of inverse length. Applying our constraint of periodicity 'a' to μ, the general form of the wavefunction can be written as a sum of products of e^{nika} and various basis states $\phi(x)$:

$$\begin{aligned} \Psi &= e^{ika}\phi_1(x) + e^{2ika}\phi_2(x) + e^{3ika}\phi_3(x) + \dots \\ &= \sum_n e^{nika}\phi_n(x) \end{aligned} \tag{2.16}$$

This is the general Bloch wavefunction for periodic crystals. To find the energy eigenstates of this Bloch wavefunction at a given wavevector value 'k', we can take the expectation value of the Hamiltonian:

$$\begin{aligned} E_k &= \int \Psi(k)^* H \Psi(k) dx \\ &= \int \sum_m e^{-mika} \phi_n^*(x) H \sum_n e^{nika} \phi_m(x) dx \\ &= \sum_n \sum_m e^{i(n-m)ka} \int \phi_m^*(x) H \phi_n(x) dx \end{aligned} \tag{2.17}$$

The term $\phi_m^*(x) H \phi_n(x)$ is an overlap integral between basis states in different lattice sites, and the sum carries over every pair of unit cells in the lattice. To simplify, we can introduce two approximations:

$$\begin{aligned} \text{if } n = m \rightarrow \phi_m^*(x) H \phi_n(x) = \alpha \\ \text{if } |n - m| = a \rightarrow \phi_m^*(x) H \phi_n(x) = \beta \end{aligned} \tag{2.18}$$

where α and β are constants in the case of this simple 1D lattice. The condition of $n = m$ corresponds to the overlap of the unit cell wavefunction with itself, to which we assign a value of α. The condition $|n - m| = a$ corresponds to n and m being nearest-neighbor sites, and we can assign the same value of β to unit cells in either direction since the interactions are identical. Equation 2.18 for a 1D lattice can then be simplified to:

$$E_k = \alpha + \beta e^{ika} + \beta^* e^{-ika} \tag{2.19}$$

This is referred to as the 'tight-binding' approximation, since it only considers interactions between each cell and its nearest neighbors. The tight binding approximation can be extended to 2D systems by considering vector-valued wavevectors and lattice translation vectors 'r':

$$E_{\mathbf{k}} = \alpha + \beta e^{i\mathbf{k}\cdot\mathbf{r}} + \beta^* e^{-i\mathbf{k}\cdot\mathbf{r}} \tag{2.20}$$

With the eight nearest-neighbors in a 2D lattice with lattice constants 'a' and 'b', this can be written as:

$$\begin{aligned} E_k = \alpha + \beta e^{ik_x a} + \beta' e^{-ik_x a} + \gamma e^{ik_y b} + \gamma' e^{-ik_y b} + \delta_1 e^{ik_x a + ik_y b} + \\ \delta_1' e^{-ik_x a - ik_y b} + \delta_2 e^{ik_x a - ik_y b} + \delta_2' e^{-ik_x a + ik_y b} \end{aligned} \tag{2.21}$$

where γ and δ correspond to the nearest neighbors in the 'y' direction and the diagonals, respectively (see Fig. 2.3). The effect of multiple basis functions per unit cell can be added by using matrix-valued coefficients which contain the interaction parameters between every two orbitals in each unit cell.

2.1.4 Zone Folding

The method presented in section 2.2 requires that the unit cell of the channel material is orthorhombic, such that it can be tiled across the rectangular device channel. However, the 2D materials studied in this thesis have structures are either hexagonal (in the case of MoS_2) or trigonal (in the case of $PtSe_2$).

To satisfy this, we use orthorhombic 'supercells' which in place of unit cells. The corresponding supercell in k-space is a rectangle which is contained within the hexagonal Brillouin zone. The repeated rectangular cell in k-space then contains parts of the original hexagonal Brillouin zone

which are 'folded' into it. This zone folding is shown schematically in Fig. 2.2a and b. An example for the hexagonal primitive cell (2.2c) and orthorhombic supercell (2.2d) bandstructures are shown in 2.2b.

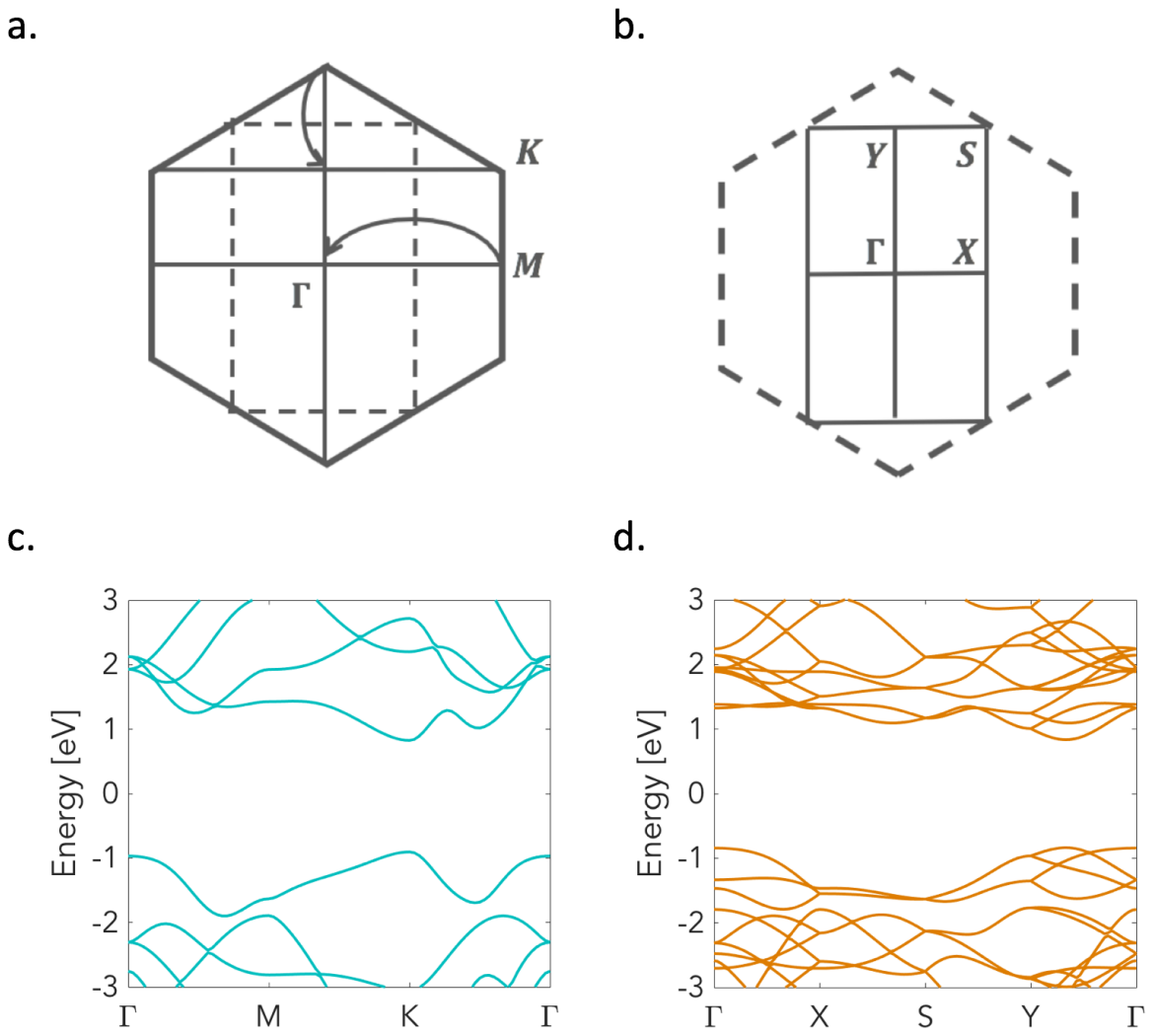

Figure 2.2: First brillouin zone of a hexagonal unit cell (a), with zone folding to the corresponding rectangular cell (b) indicated with arrows. The bandstructures for the hexagonal unit cell and rectangular supercell are shown in (c), and (d) respectively.

2.1.5 Complex Energy Eigenstates

To solve for the real-valued energy solutions of the tight-binding Hamiltonian (Eqn.2.21), we can simply evaluate it at a specified real-values points in k-space. However, the full set of energy eigenvalues includes complex-valued solutions which have real-part energy values within the material bandgap, and correspond to spatially decaying wavefunctions. To include these solutions, a different approach is needed. We start by writing out the eigenvalue equation for the Hamiltonian:

$$[H]\Psi = E\Psi \tag{2.22}$$

The nearest-neighbors for a rectangular supercell are shown in Fig.2.3, which uses the following lattice vectors:

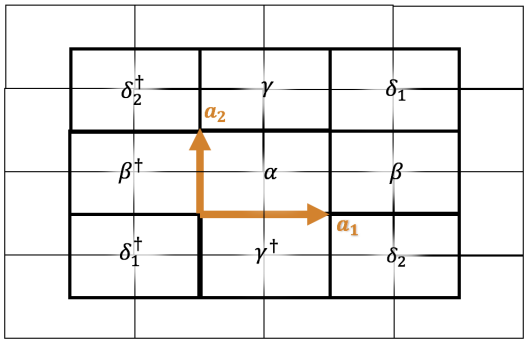

Figure 2.3: Schematic of all nearest neighbors (cells with bold outline) for a rectangular lattice with orthogonal basis vectors a_1 and a_2.

With the lattice vectors:

$$\begin{aligned} a_1 &= a \cdot \begin{bmatrix} 1 \\ 0 \end{bmatrix} \\ a_2 &= b \cdot \begin{bmatrix} 0 \\ 1 \end{bmatrix} \end{aligned} \tag{2.23}$$

Which leads to the nearest-neighbor tight binding Hamiltonian:

$$\begin{aligned} [H]\Psi = [\alpha + \beta e^{ik_x a} + \beta' e^{-ik_x a} + \gamma e^{ik_y b} + \gamma' e^{-ik_y b} + \delta_1 e^{ik_x a + ik_y b} + \\ \delta_1' e^{-ik_x a - ik_y b} + \delta_2 e^{ik_x a - ik_y b} + \delta_2' e^{-ik_x a + ik_y b}]\Psi = E\Psi \end{aligned} \tag{2.24}$$

Where α, β, etc are matrices containing the interaction parameters between the unit cells and their nearest neighbors, as described in the previous section. The size of each of these NxN

matrices is N = (# atoms per unit cell)×(# basis functions per atom) = (# basis functions per unit cell). For the MoS_2 rectangular cell with 2 Mo atoms (containing 5 basis functions each based on the 5 d orbitals) and 4 S atoms (containing 3 basis functions each based on the 3 p orbitals), each matrix would be N = $(5 \times 2) + (4 \times 3) = 22$.

We will solve for all the values of the wavevector k_x at pre-specified values of k_y. So gather the terms related to k_x:

$$\begin{aligned}[H]\Psi = [(\beta + \delta_1 e^{ik_y b} + \delta_2 e^{-ik_y b})e^{ik_x a} + (\beta' + \delta_1' e^{-ik_y b} + \delta_2' e^{ik_y b})e^{-ik_x a} \\ +(\alpha + \gamma e^{ik_y b} + \gamma' e^{-ik_y b})]\Psi = E\Psi\end{aligned} \tag{2.25}$$

Redefine some terms to simplify:

$$\begin{aligned}\hat{\alpha} &\leftarrow (\alpha + \gamma e^{ik_y b} + \gamma' e^{-ik_y b}) \\ \hat{\beta} &\leftarrow (\beta + \delta_1 e^{ik_y b} + \delta_2 e^{-ik_y b}) \\ \hat{\beta}' &\leftarrow (\beta' + \delta_1' e^{-ik_y b} + \delta_2' e^{ik_y b})\end{aligned} \tag{2.26}$$

$$[H]\Psi = [\hat{\alpha} + \hat{\beta} e^{ik_x a} + \hat{\beta}' e^{-ik_x a}]\Psi = E\Psi \tag{2.27}$$

Define $\lambda = e^{ik_x a}$, so that $\lambda^2 = e^{2ik_x a}$ and $\lambda^0 = 1$

$$[\hat{\beta}\lambda^2 + (\hat{\alpha} - EI)\lambda^1 + \hat{\beta}'\lambda^0]\Psi = 0 \tag{2.28}$$

This polynomial eigenvalue equation can be solved for all values of λ with a standard QZ factorization algorithm, such as the one used by MATLAB's 'polyeig()' function. The solutions for k_x can then be calculated using $k_x = -i\frac{1}{a}log(\lambda)$.

For a hexagonal cell with lattice constant 'a' and lattice vectors as shown in Fig.2.4:

The lattice vectors for the zigzag cell (figure 2.4a) are:

$$\begin{aligned}a_1 &= a_0 \cdot \begin{bmatrix}1 \\ 0\end{bmatrix} \\ a_2 &= a_0 \cdot \begin{bmatrix}-1/2 \\ \sqrt{3}/2\end{bmatrix}\end{aligned} \tag{2.29}$$

We can condense some of the full expression for the tight binding hamiltonian 'H' into 'h' and its transpose:

$$[H]\Psi = [\alpha + h + h']\Psi = E\Psi \tag{2.30}$$

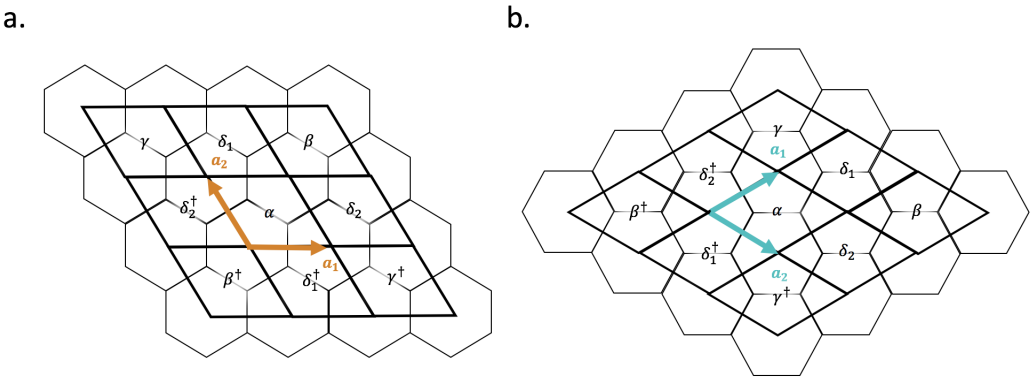

Figure 2.4: Schematic of all nearest neighbors (cells with bold outline) for a (a) zigzag and (b) armchair hexagonal lattice with basis vectors a_1 and a_2.

$$\begin{aligned} h &= \beta e^{i[k_x\ k_y]\cdot(a_1+a_2)} + \gamma e^{i[k_x\ k_y]\cdot(a_1-a_2)} + \delta_1 e^{i[k_x\ k_y]\cdot(a_1)} + \delta_2 e^{[k_x\ k_y]\cdot(a_2)} \\ &= \beta e^{i[k_x\ k_y]\cdot\begin{bmatrix}1/2\\ \sqrt{3}/2\end{bmatrix}a} + \gamma e^{i[k_x\ k_y]\cdot\begin{bmatrix}3/2\\ -\sqrt{3}/2\end{bmatrix}a} + \delta_1 e^{i[k_x\ k_y]\cdot\begin{bmatrix}1\\ 0\end{bmatrix}a} + \delta_2 e^{[k_x\ k_y]\cdot\begin{bmatrix}-1/2\\ \sqrt{3}/2\end{bmatrix}a} \end{aligned} \tag{2.31}$$

To simplify, let's set k_y to zero, such that our energy eigenvalue solutions will be constrained to the k_x axis:

$$h = \beta e^{\frac{1}{2}ik_x a} + \gamma e^{\frac{3}{2}ik_x a} + \delta_1 e^{ik_x a} + \delta_2 e^{-\frac{1}{2}ik_x a} \tag{2.32}$$

Plug this into Eqn.2.30:

$$\begin{aligned} &[\alpha + \beta e^{\frac{1}{2}ik_x a} + \gamma e^{\frac{3}{2}ik_x a} + \delta_1 e^{ik_x a} + \delta_2 e^{-\frac{1}{2}ik_x a} \\ &+\beta' e^{-\frac{1}{2}ik_x a} + \gamma' e^{-\frac{3}{2}ik_x a} + \delta_1' e^{-ik_x a} + \delta_2' e^{\frac{1}{2}ik_x a} - EI]\Psi = 0 \end{aligned} \tag{2.33}$$

Now we can define a parameter $\lambda = e^{\frac{1}{2}ik_x a}$ and collect factors of λ:

$$[\gamma'\lambda^{-3} + \delta_1'\lambda^{-2} + (\beta' + \delta_2)\lambda^{-1} + (\alpha - EI)\lambda^0 + (\beta + \delta_2')\lambda^1 + \delta_1\lambda^2 + \gamma\lambda^3]\Psi = 0 \tag{2.34}$$

Multiply out by λ^3:

$$[(\gamma')\lambda^0 + (\delta_1')\lambda^1 + (\beta' + \delta_2)\lambda^2 + (\alpha - EI)\lambda^3 + (\beta + \delta_2')\lambda^4 + (\delta_1)\lambda^5 + (\gamma)\lambda^6]\Psi = 0 \tag{2.35}$$

Doing the same for the zigzag cell (Fig. 2.4b) with the following lattice vectors gives the eigenvalue equation:

$$b_1 = a_0 \cdot \begin{bmatrix} 3/2 \\ \sqrt{3}/2 \end{bmatrix}$$
$$b_2 = a_0 \cdot \begin{bmatrix} 3/2 \\ -\sqrt{3}/2 \end{bmatrix} \tag{2.36}$$

$$[(\beta')\lambda^0 + (\delta_2' + \delta_1')\lambda^3 + (\alpha - EI + \gamma + \gamma')\lambda^6 + (\delta_2 + \delta_1)\lambda^9 + (\beta')\lambda^{12}]\Psi = 0 \tag{2.37}$$

Similarly to Eqn.2.28, Eqns.2.35 and 2.37 can be solved for all λ by QZ factorization, and then $k_x = -2i\frac{1}{a}log(\lambda)$. Figure 2.5 shows the solutions of k_x up the edge of the first Brillouin zone for a 6 eV energy range around the midgap, for both the armchair and zigzag cell. The real values (plotted on the right side of each graph) are the energies of the stable eigenstates of the tight binding Hamiltonian. The complex-numbered solutions correspond to unstable or decaying states, and the imaginary part of each complex solution (plotted on the left side of each graph) is proportional to the lifetime of a carrier in that state. This scheme can be easily extended to include more nearest neighbors if more tight-binding interactions are needed to accurately reproduce the DFT bandstructure.

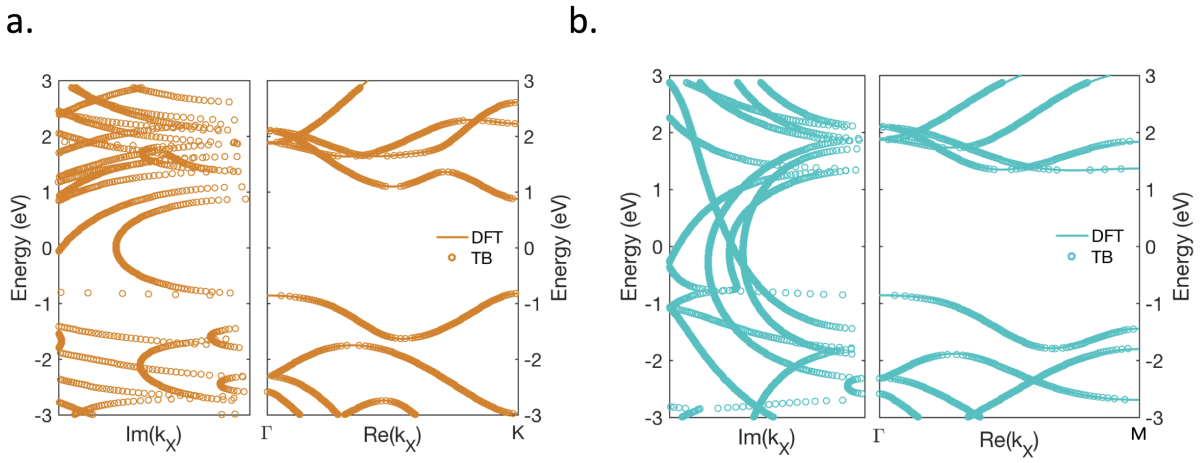

Figure 2.5: Real and imaginary bandstructure as a function of k_x for the (a) armchair and (b) zigzag cells, which have the unit cells shown in figure 2.4. These are plotted to the edge of the Brillouin zone along the k_x axis, which for the armchair cell is the 'K' high symmetry point and for the zigzag cell is the 'M' point.

2.1.6 Monolayer Dielectric Constants

The self-consistent NEGF-Poisson Framework which will be discussed in section 2.2 uses Poisson's equation to solve for the electrostatic potential $U(x)$ along the device channel 'x' when given an electron charge density $\rho(x)$:

$$\nabla \cdot [\nabla U] = \frac{q}{\varepsilon}\rho(x) \tag{2.38}$$

Where $\epsilon = \epsilon_r \epsilon_0$ is the static dielectric constant of the material, which characterizes its polarizability in response to an applied field. The value of the dielectric constant ϵ_r used here significantly affects the variation of electrostatic potential between the contacts and the channel. In this thesis, the dielectric constants for monolayer TMDs are extracted from ab-initio DFT calculations. We use an ion-clamped approximation which neglects atomic displacements.

The electronic (high frequency) contributions to the dielectric constant can be directly calculated for the monolayer+vacuum supercell using Quantum Espresso's ph.x function. This gives us the following tensor:

$$\epsilon^{SC} = \begin{bmatrix} \epsilon_{\parallel}^{SC} & 0 & 0 \\ 0 & \epsilon_{\parallel}^{SC} & 0 \\ 0 & 0 & \epsilon_{\perp}^{SC} \end{bmatrix} \tag{2.39}$$

Where ϵ^{SC} is the dielectric constant of the supercell, which consists of a monolayer TMD plus the "vacuum space" to separate it from its periodic images in the z-axis. $\epsilon_{\parallel}^{SC}$ is the in-plane permittivity of this supercell, and $\epsilon_{\parallel}^{SC}$ is its out-of-plane permittivity, perpendicular to the 2D monolayer. These supercell dielectric constants are influenced by the individual anisotropic permittivities of the monolayer ϵ^m and the vaccuum relative permittivity $\epsilon^{vac} = 1$. To extract the dielectric constants for only the monolayer, we can employ basic capacitor models as shown in Fig.2.6.

In the out-of-plane direction, $\epsilon_{\perp}^{SC}$ is treated as a series combination of the monolayer capacitance C^m and vacuum capacitance C^{vac} (Fig.2.6a):

$$\frac{1}{C_{SC}} = \frac{1}{C_{vac}} + \frac{1}{C_m} \tag{2.40}$$

This can be written in terms of the permittivities, relative thicknesses, and areas:

$$\frac{c}{\epsilon_{\perp}^{SC} A} = \frac{c-t}{\epsilon_{\perp}^{vac} A} + \frac{t}{\epsilon_{\perp}^{m} A} \tag{2.41}$$

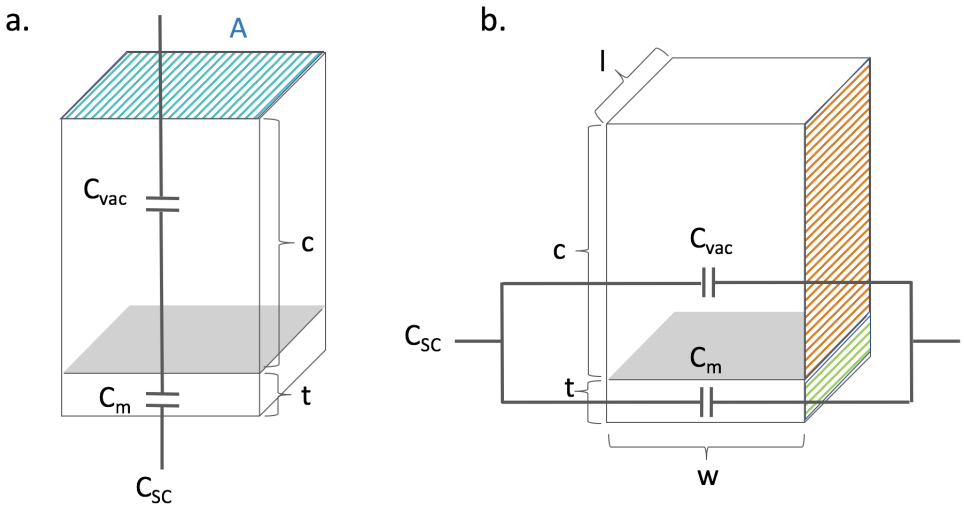

Figure 2.6: Schematic representations of how the (a) out-of-plane and (b) in-plane supercell capacitances can be written as (a) series or (b) parallel combinations of the monolayer and vacuum capacitances. The grey section at the bottom of the supercell indicates the monolayer material.

Where c is the total thickness of the supercell, t is the thickness of the TMD monolayer, and A is the out-of-plane area of the supercell. Solving this equation for $\epsilon_{\perp}^{m}$, we get:

$$\epsilon_{\perp}^{m} = \frac{1}{\frac{c}{t}(\frac{1}{\epsilon_{\perp}^{SC}} - 1) - 1} \tag{2.42}$$

The in-plane permittivity can be similarly treated as a parallel combination of the two capacitances (Fig.2.6b):

$$C_{SC} = C_{vac} + C_m \tag{2.43}$$

$$\frac{\epsilon_{\parallel}^{SC} cl}{w} = \frac{\epsilon_{\parallel}^{vac}(c-t)l}{w} + \frac{\epsilon_{\parallel}^{m} tl}{w} \tag{2.44}$$

Where l and w are the length and width of the supercell. Once again solving for $\epsilon_{\parallel}^{m}$:

$$\epsilon_{\parallel}^{m} = 1 + \frac{c}{t}(\epsilon_{\parallel}^{SC} - 1) \tag{2.45}$$

Equations 2.42 and 2.45 can be used to remove the contributions of the vacuum from the supercell permittivity. However, there is a notable difficulty in determining the value of the monolayer thickness 't' for a 2D TMD. To start, we can identify a range of possible values: t must be greater than the intralayer chalcogen spacing (S - S in MoS_2) but less than the interlayer transition metal spacing (Mo - Mo in MoS_2) (see Fig.2.7a). Although $\epsilon_{\parallel}$ is only slightly dependant on 't' within such a small range, $\epsilon_{\perp}$ can vary over an order of magnitude. Therefore, selecting a thickness within this range is non-trivial.

To introduce a more consistent thickness and dielectric constant for 2D materials, Ref [28] defines an "effective isotropic model" in which the 't' used is the thickness obtained by setting $\epsilon_{\parallel} = \epsilon_{\perp}$. Fig.2.7b illustrates this method using the extracted dielectric tensor for monolayer MoS_2.

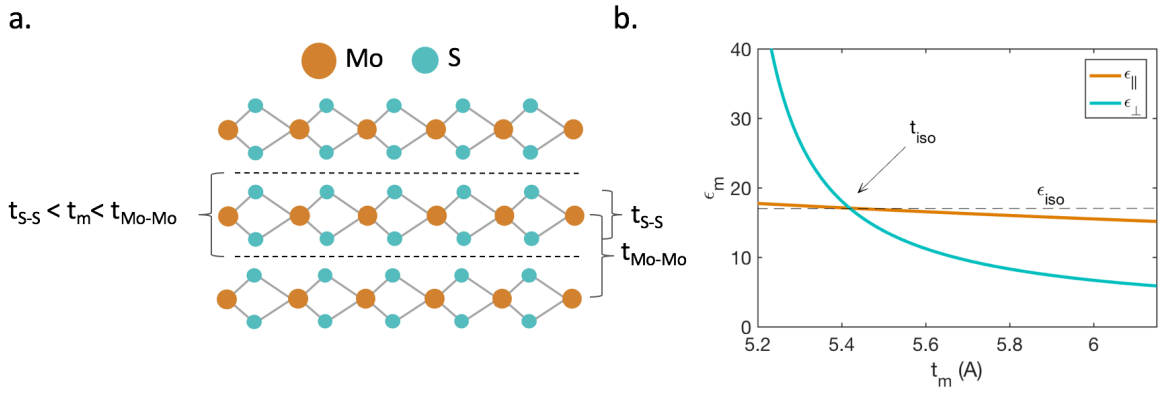

Figure 2.7: (a) Schematic of three stacked MoS_2 monolayers pictured in side-view, where the interlayer transition metal spacing (t_{Mo-Mo}) and intralayer chalcogen spacing (t_{S-S}) are pictured, along with a probable value for the monolayer thickness t_m. (b) The in-plane ($\epsilon_{\parallel}$) and out-of-plane ($\epsilon_{\perp}$) dielectric constants of monolayer MoS_2 in the 2D phase as shown in (a), plotted as a function of monolayer thickness as used in 2.42 or 2.45. The thickness at which the system becomes isotropic is t_{iso}. The upper bound on the 't' axis corresponds to t_{Mo-Mo}.

At the extracted t_{iso} of 0.54 nm, $\epsilon^m_{\perp} = \epsilon^m_{\parallel} = \epsilon^m_{iso} = 17.0598$, which is in close agreement with previous literature [28] [20]. This value of ϵ^m_{iso} is also independent of the supercell thickness used to calculate t_{iso}. The ionic (low frequency) contributions of the dielectric constants, which include the atomic displacements resulting from an applied electric field, can also be calculated with Density Functional Perturbation Theory (DPFT) via Quantum Espresso's dynmat.x function. However, these are generally less significant for 2D materials [29].

2.2 The NEGF-Poisson Transport Framework

The eigenstates of an isolated system can be solved by the Schroedinger Equation:

$$\begin{aligned} H\left|\Psi\right\rangle &= E\left|\Psi\right\rangle \\ \left[EI - H\right]\left|\Psi\right\rangle &= 0 \end{aligned} \tag{2.46}$$

Where H is the Hamiltonian, and E are the energies corresponding to the eigenstates $|\Psi\rangle$. In the case of a non-isolated system with open boundary conditions, we can add an additional source term S:

$$\left[EI - H - \Sigma\right]\left|\Psi\right\rangle = \left|S\right\rangle \tag{2.47}$$

Where Σ is a self-energy term which renormalizes the energies of the channel in the presence of the inflow from S. $[EI - H - \Sigma]^{-1}$ is the Green's function of the Hamiltonian, G, which describes how the eigenstates respond to the boundary conditions.

This formalism can be used to model a transistor channel under ballistic conditions, using a discrete matrix representation. For this, the channel potential U (which is calculated under the influence of the drain and gate biases) can be included in the Green's function, and the self-energy can be split into two terms to account for the existence of the source (Σ_s) and drain (Σ_d):

$$G(E) = \left[(E + i0^+)I - H - U - \Sigma_s - \Sigma_d\right]^{-1} \tag{2.48}$$

where $i0^+$ is a small imaginary value which shifts the poles of G(E) into the complex plane to avoid numerical instabilities. U is a diagonal square matrix such that $U(x, x)$ is the channel potential at point x. The matrices which make up the tight-binding hamiltonian:

$$h = \alpha + \beta e^{i\mathbf{k}\cdot\mathbf{r}} + \beta^* e^{-i\mathbf{k}\cdot\mathbf{r}} \tag{2.49}$$

are assembled into a hamiltonian which describes the entire channel (and used in Eqn.2.48):

$$H = \begin{pmatrix} \alpha & \beta & 0 & \cdots & 0 \\ \beta^+ & \alpha & \ddots & \ddots & \vdots \\ 0 & \ddots & \ddots & \ddots & 0 \\ \vdots & \ddots & \ddots & \alpha & \beta \\ 0 & \cdots & 0 & \beta^+ & \alpha \end{pmatrix} \tag{2.50}$$

where each α matrix along the diagonal corresponds to an atomic site along the real-space dimension of the channel. Other nearest neighbor matrices are included within α and β.

Just as the Hamiltonian specifies the properties of an isolated system, all the relevant quantities for this non-isolated system can be extracted from the Green's function. The diagonal of the anti-Hermitian part of the Green's function, calculated with

$$A(E) = i[G - G^+] \tag{2.51}$$

gives the density of states along the real-space direction of the device, such that $Tr(A)$ is the total density of electronic states available. We define two other matrices which extract the anti-Hermitian parts of the self-energy matrices:

$$\begin{aligned} \Gamma_s &= i(\Sigma_s - \Sigma_s^+) \\ \Gamma_d &= i(\Sigma_d - \Sigma_d^+) \end{aligned} \tag{2.52}$$

These quantities can be used to calculate the transmission across the channel:

$$T(E) = Tr(\Gamma_s G \Gamma_d G^+) \tag{2.53}$$

And when multiplied by the availability of states across the channel, which can be found using the fermi functions in the source (f_s) and drain (f_s), and the charge (x2 for spin), this gives us the current at that energy:

$$I(E) = \frac{2q}{h} T(E)(f_s(E) - f_d(E)) \tag{2.54}$$

The total current is just this value integrated over all energies. The electron and hole densities across the channel are found by:

$$\begin{aligned} n &= 2 \int \frac{dE}{2\pi} G \Gamma_s G^+ \\ p &= 2 \int \frac{dE}{2\pi} G \Gamma_d G^+ \end{aligned} \tag{2.55}$$

Using these values of n and p, the channel potential U can then be solved using Poisson's Equation:

$$\nabla \cdot [\varepsilon_r \nabla U] = \frac{q}{\varepsilon_0}[N_D - N_A - n + p] \tag{2.56}$$

where N_D and N_A are the chosen donor and acceptor concentrations as a function of the device length, and ε_r is the static dielectric constant of the channel. The effects of the source, drain, and gate electrodes can be included as boundary conditions when solving this equation in a finite-difference scheme. Equations 2.48 and 2.56 are then solved self-consistently until both the channel potential and charge vary minimally across iterations. At that point, the current can be calculated using Eqn.2.54.

3

Designing an Ultra-sensitive Grounded-Gate Photodiode

***Statement of Contributions**: The work in this chapter is adapted from the journal article "Ultrasensitive Multilayer MoS_2-Based Photodetector with Permanently Grounded Gate Effect", which was published in Advanced Electronic Materials in Febuary 2020 [30]. As an equal-contributing author, I preformed all of the simulations within this paper, prepared figures 1a-b, 2b-d, 3a-b, and 6a-b, and wrote the corresponding sections, assisted by Richard Han from the University of Waterloo. The device fabrication and collection of all experimental data was done by Mohammed Naqi, Sooho Choo, Sangjin Kang, and Jeonghun Kim from Sungkyunkwan University. The project was supervised by Prof. Youngki Yoon (University of Waterloo) and Prof. Sunkook Kim (Sungkyunkwan University).*

3.1 Background

A single monolayer of MoS_2 has an optical absorption several times higher than that of bulk silicon. [31] Due to these strong light-matter interactions, it has been explored as a candidate material for optoelectronics, and several studies have reported high-performance MoS_2 photodetectors [32, 33, 34, 35, 36, 37].

MoS_2 photodetectors have been designed using intrinsic P-I-N junctions (shown schematically in Fig.3.1(a)), P-N heterojunctions (Fig.3.1(b)), and Schottky-barrier devices with metal contacts

(Fig.3.1(c)). In the first two cases, photogenerated carriers can be efficiently separated at the junctions, leading to a higher photoresponse compared to the third case in which this process occurs in the intrinsic material. However, intrinsic junctions must be formed using either a chemical, elemental, or electrostatic doping method. Although techniques have been developed to perform this, doping remains a significant experimental challenge in the construction of 2D material devices. Chemical doping techniques are highly dependent on environmental conditions, [38, 39] elemental doping causes limited vertical junction formation which leads to lower charge mobility, [40] and the electrostatic doping method has led to devices with low photoresponses due to the additional electric fields. [41]

Heterojunction photodiodes with dissimilar materials have also been studied, using MoS_2/Si, [42, 43] MoS_2/GaN, [44] MoS_2/graphene, [45, 46] MoS_2/Black Phosphorus, [47, 48] and MoS_2/pentacene, [49, 50] and show improved electrical and optical properties compared to homojunction photodiodes. However, despite notable performance improvements in terms of photoresponsivity and sensitivity, homo- and heterojunction photodiodes are limited by low carrier mobility, difficult processing techniques, and unstable photoresponsive behavior. [51, 52] They are also limited by the quality of the interface, which is highly dependent on the fabrication methods used to make them.

Schottky-barrier diodes with instrinsic channels are a more experimentally accessible device structure for these photodetectors. [53, 54] In this case, a voltage applied across the two metal contacts encourages the separation of photogenerated carriers, while the Schottky barriers present at the metal-MoS_2 interfaces discourage the injection of carriers into the channel, which therefore suppresses 'dark' current. However, although the presence of the Schottky barriers discourages thermionic current it is still possible for carriers to tunnel into the channel. Since the sensitivity of a photodetector depends on its ability to deliver current under illumination while suppressing current under dark conditions, this results in a lower sensitivity overall.

Figure 3.1: (a) Schematic of a p-i-n junction with two p-type and n-type contacts separated by an intrinsic, un-doped layer. Carriers which are generated within the intrinsic layer are seperated by a field across the terminals, and drift to the contacts. (b) Schematic of a p-n junction, consisting of a p-type and n-type region. Photogenerated carriers at the junction are seperated by the staggered band alignment. (c) A schematic of a Schottky-barrier diode, which is made with an intrinsic material contacted with two metals. Carriers are generated in the instrinsic region and collectd by the metal contacts.

In this work we introduce a device design which overcomes the reduced sensitivity of the intrinsic schottky-barrier photodiode without introducing complicated fabrication processes. This is done by reducing the dark current by introducing rectifying behaviour at the source-channel junction, using a "grounded-gate design". This strategy relies heavily on the atomic-thinness of the MoS_2 channel, which allows for a high level of control over the source-channel and channel-drain tunneling barriers. The physics and operation of the device are presented in the next section.

3.2 Device Design and Operation

Figure 3.2(c) outlines the device architecture which we used, which is a compromise between a three-terminal phototransistor (Fig.3.2(a)) and a two-terminal photodiode (Fig.3.2(b)). Rather than explicitly including a third contact, the 'gate' terminal is shorted to the source contact, which is then grounded. This has a similar electrostatic effective to that of a gate terminal, while avoiding the additional complexity of a three-terminal device.

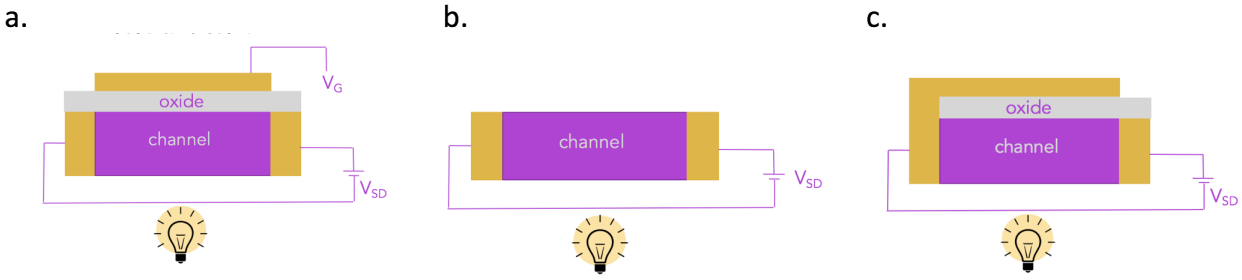

Figure 3.2: (a) Schematic of a conventional three-terminal phototransistor. (b) Schematic of a two-terminal photodiode. (c) Schematic of the 'grounded-gate' photodetector introduced in this work, where the source terminal extends over the channel to resemble a gate contact and introduce rectification at one end.

The rectification effect caused by the presence of a grounded-gate terminal serves to increase the photosensitivity of the device by decreasing the dark current under the forward bias condition. This can be seen clearly by comparing it to a regular two-terminal M-S-M photodetector, in which the energy bands are symmetric under forward and reverse bias. Figure 3.3 displays the band diagrams for both of these cases, which can be used to investigate current flow in the device in each state of operation. The band diagrams of the two-terminal photodetector are symmetric for both reverse and forward bias, and in both cases there is a non-negligible amount of current which can tunnel into the channel under dark conditions.

Meanwhile for the grounded-gate design under reverse bias, the energy barrier created at the gate-drain junction is sharp enough to allow for tunneling current in the same direction as the

photocurrent. However, in forward bias, the energy barrier at the source-gate junction is too wide to permit tunneling current and high enough to prevent significant thermionic current, while photocurrent is unobstructed.

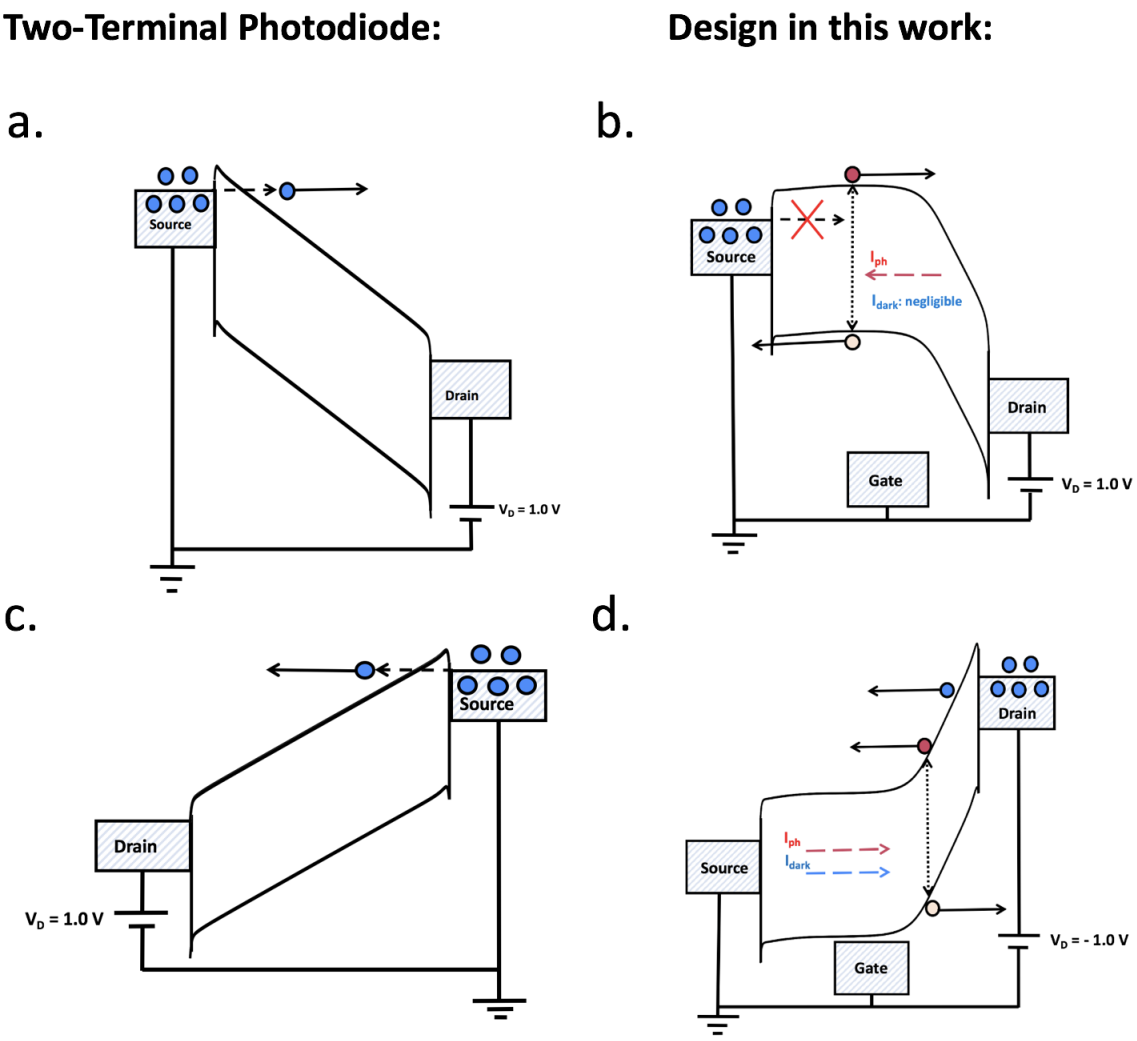

Figure 3.3: Band structures of a two terminal metal-semiconductor-metal device ((a), (c)) and the grounded-gate device ((b), (d)) under forward bias ((a), (b)) and reverse bias ((c), (d)) of +1 V. The two-terminal device shows lack of tunneling current suppression. Adapted from Ref [30]

3.3 Simulated Device Details

Dark current in the device was simulated using the non-equilibrium Green's function (NEGF) formalism with electrostatics described by the Poisson equation. The simulated device structure was a Schottky barrier FET with a Schottky barrier height of $\Phi_{Bn} = 0.1$ eV, and a 40 nm-long monolayer MoS_2 channel. A 20 nm gate was used with 10 nm gate underlap on each side. The gate oxide was 2.5 nm thick SiO_2. These model parameters (Schottky barrier height, gate metal work function) were found such that the simulated I_D–V_D characteristics (which are shown later in Fig.3.7(b)) resemble the corresponding experimental data (Fig.3.7(a)).

The Hamiltonian for the NEGF transport solver was constructed using an effective mass approximation ($m^* = 0.45m_0$). Due to the relatively short channel length, ballistic transport was assumed through the channel. The photoconductive effect was considered to calculate photocurrent (I_{ph}), using: [55]

$$I_{ph} = \frac{A_{ch}}{L_{ch}} V_D \Delta\sigma \tag{3.1}$$

Where A_{ch} is the cross-sectional area of the channel, $\Delta\sigma = q\mu\Delta n$ is the conductivity of the material, μ is the carrier mobility, and Δn is the density of photogenerated carriers. The excess carrier density is calculated with $\Delta n = g\tau_r$ where $g = \eta P_{abs}/h\nu$ is the generation rate, and τ_r is the carrier recombination lifetime. η and $h\nu$ are the internal quantum efficiency and the single photon energy, and P_{abs} is the absorbed power density which was calculated using $P_{abs} = P_{inc}[1 - e^{a_\perp d} + e^{a_\parallel d}]$. $e^{a_\perp d}$ and $e^{a_\parallel d}$ are the absorption coefficients in the vertical and lateral directions, d is the thickness of monolayer MoS_2, and P_{inc} is the incident optical power density.

3.4 Results

3.4.1 Simulation Results

To illustrate the device operation, Fig.3.4 presents the simulated I_D–V_D characteristics, where at positive drain voltages, the dark current for the grounded-gate photodiode is negligible but that of the two-terminal device is steadily increasing. Without a gating effect under forward bias to obstruct dark current flow, tunneling current is significant as compared to that with the grounded-gate photodiode. The addition of the gate terminal adds the capability to have a preset modulation of the potential along the channel without needing to operate it as a three-terminal device.

To further improve the photodetection capabilities of this design, two areas could be targeted; increasing the photocurrent by making the generation of excess carriers more efficient, or suppressing dark current. Since the former can be investigated experimentally by varying wavelength

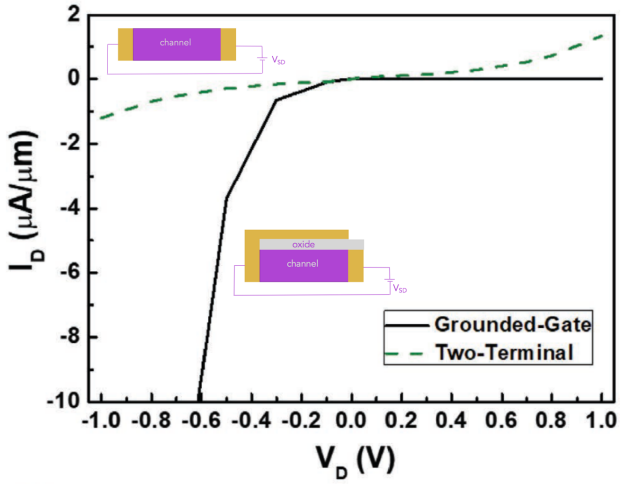

Figure 3.4: Electrical characteristics (dark current) of both the proposed grounded-gate photodiode (solid black lines) and a two-terminal device (dashed green lines). Adapted from Ref [30].

and incident power density, here we focus on the suppression of the dark current to increase the sensitivity of the photodetector while leaving the photocurrent unchanged.

In principle, for three-terminal devices, dark current can be suppressed by increasing the channel potential barrier through gate voltage modulation. A similar effect can be achieved in the presented grounded-gate device by choosing a gate metal with a different work function, defined as $\Phi_m = -e\Phi_V - E_F$, where Φ_V is the electrostatic potential of the vacuum and E_F is the Fermi level of the metal. For the device simulations preformed here, a nominal gate metal work function Φ_m^0 was used for the photodiode design.

Figure 3.5(a) presents the effect of changing the gate metal work function with respect to Φ_m^0 on the dark current of the photodiode. When increased (eg $\Phi_m - \Phi_m^0 > 0$ eV), the energy barrier for electron injection from the source to the channel under forward bias is increased, which further suppresses the thermionic current. This reduction in dark current serves to improve the sensitivity of the design. Figure 3.5(b) presents the change in sensitivity based on the simulated range of the variation of gate metal work function. Notably, an increase of 0.20 eV causes over three orders of magnitude of increase in the sensitivity. Therefore, the device design can be optimized to detect very low levels of light by using a gate metal with a larger metal work function.

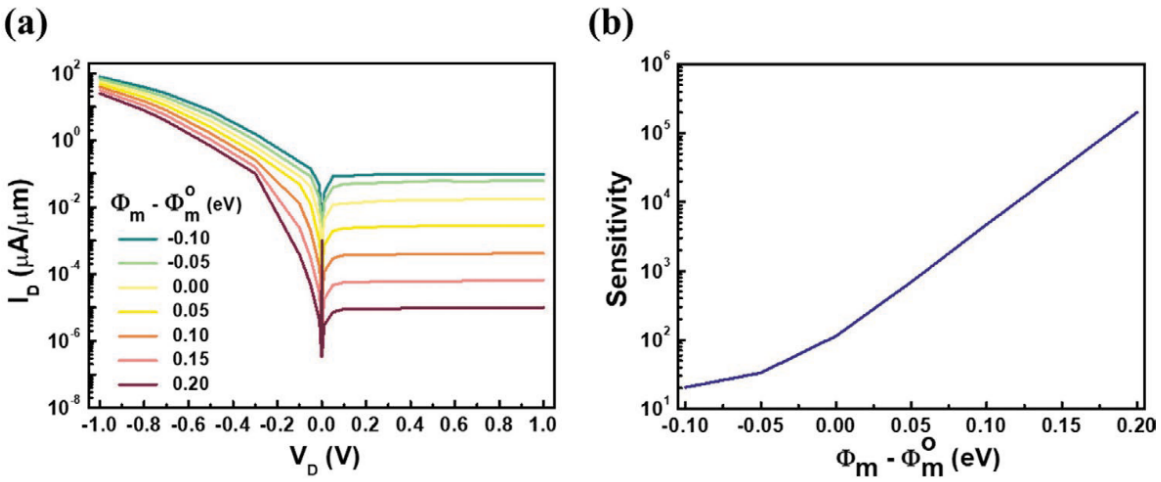

Figure 3.5: (a) Effect of changing the gate metal work function on the electrical characteristics (dark current) of the device. (b) Effect of changing the gate metal work function on the sensitivity of the grounded-gate photodiode. Adapted from Ref [30].

3.4.2 Comparison to Fabricated Device

To explore the performance under illumination, a device was experimentally fabricated and characterized under different wavelengths and intensities of light. The fabricated device uses a multilayer MoS_2 semiconductor layer between metal source and drain electrodes made of titanium and gold (Ti/Au), as well as a global bottom gate terminal which is permanently shorted to the ground contact of the source ($V_G = 0V$) following the design presented in Fig.3.2. The multilayer MoS_2 was transferred onto the global bottom-gate/dielectric (Al_2O_3) layers through mechanical exfoliation. Figure 3.6 presents a schematic outline of the fabrication process (a), and an image of the device with the MoS_2-flake channel (b).

Figure 3.7 shows a comparison of the simulated and experimental I_D-V_D curves, in which the dark current (shown in black) displays the expected rectification effect. The I_D–V_D curve has an increase in current (I_D) by three orders of magnitude under forward bias when illuminated with blue light (405 nm) with a power intensity of $430 W m^{-2}$. On the contrary, the change in current at the reverse bias is relatively insignificant under illumination. This effect is highlighted in Fig.3.8, which compares the I_D-V_D characteristics of the grounded-gate photodiode with a conventional two-terminal photodiode, following the theoretical results from Fig.3.4. As expected, the grounded-gate device shows a high level of rectification that is not present in the symmetric characteristics of the two-terminal device.

The grounded-gate device was then evaluated according to several key figures of merit for photode-

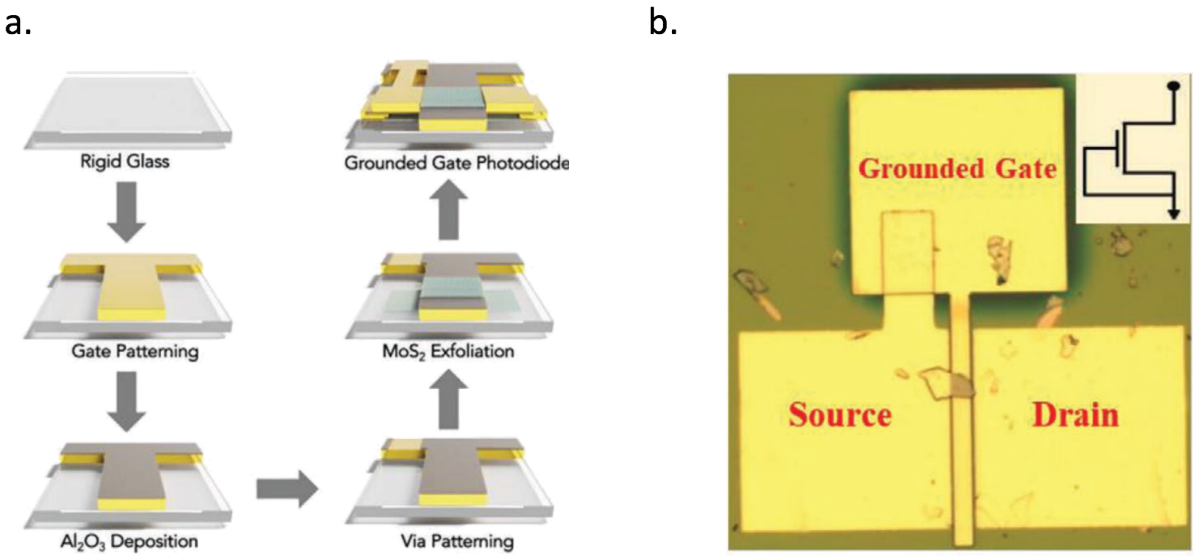

Figure 3.6: (a) A sequential fabrication process of the proposed photodiode. (b) An optical image of the photodiode. Adapted from Ref [30].

tection, such as responsivity (R), sensitivity (S) and specific detectivity (D^*). Photoresponsivity is a measure of photodetector gain, and is calculated as:

$$R = \frac{I_{ph}}{P_{inc}} \tag{3.2}$$

Photosensitivity is defined as:

$$S = \frac{I_{ph}}{I_{dark}} \tag{3.3}$$

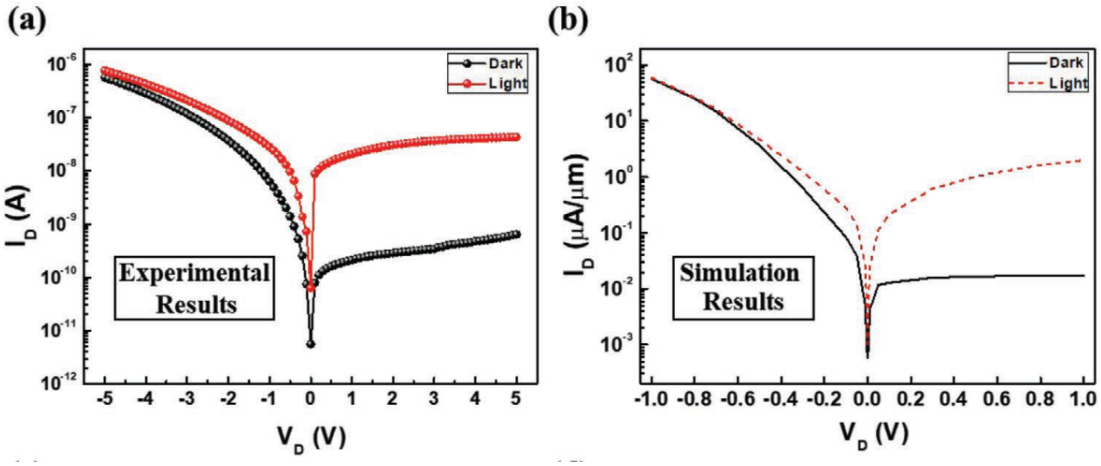

Figure 3.7: (a) Electrical measurement of the grounded-gate photodiode under dark and light illuminations (blue light (405 nm), incident power density $P_{inc} = 430Wm^{-2}$. (b) Simulated electrical measurement of the photodiode design under dark and illuminated conditions (blue light (405 nm), $P_{inc} = 430Wm^{-2}$). Adapted from Ref [30].

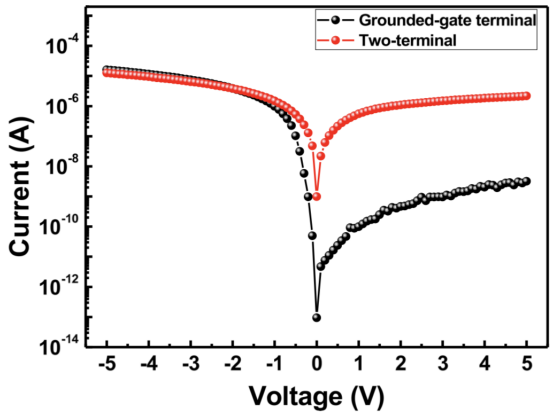

Figure 3.8: Experimental comparison of the proposed grounded-gate terminal device with the two-terminal device, showing a pronounced decrease in dark current due to the thicker tunneling barrier at the source-channel junction. Adapted from Ref [30].

Where I_{dark} represents the dark current. Photocurrent can be obtained by $I_{ph} = I_D$ - I_{dark}. Due to the dark current being the dominant source of noise in this photodetector, the sensitivity can be thought of as a signal-to-noise ratio. The specific detectivity is defined as:

$$D^* = \frac{RA_{ch}^{1/2}}{(2eI_{dark})^{1/2}} \tag{3.4}$$

Where e is the elementary charge. The responsivity and sensitivity of the photodiode were measured under blue light at various power intensities from 200 to $3mW$, and the functional relationship of photoresponsivity and light power is fitted by a power law behaviour $R = P_{inc}^{\beta-1}$ with a fitting parameter $\beta = 0.37$. Results show responsivities in the range of $0.2 - 1.1AW^{-1}$ (see Fig.3.9(a)), exhibiting high reliability in photodetection. The sensitivity was in the range of $20 - 180$ and also distinctly linear. The specific detectivity of the photodiode was measured under different wavelengths of light at an incident power of 500, which is shown in Fig.3.9(b). As the wavelength increases from blue to red, there are gradual decreases in detectivity and responsivity due to the reduced photon energy [56]. The results show linear trends in the range of $6.5 - 3.2 \times 10^{10}$ Jones for detectivity and $1.1 - 0.5AW^{-1}$ for responsivity, indicating highly sensitive and responsive performance.

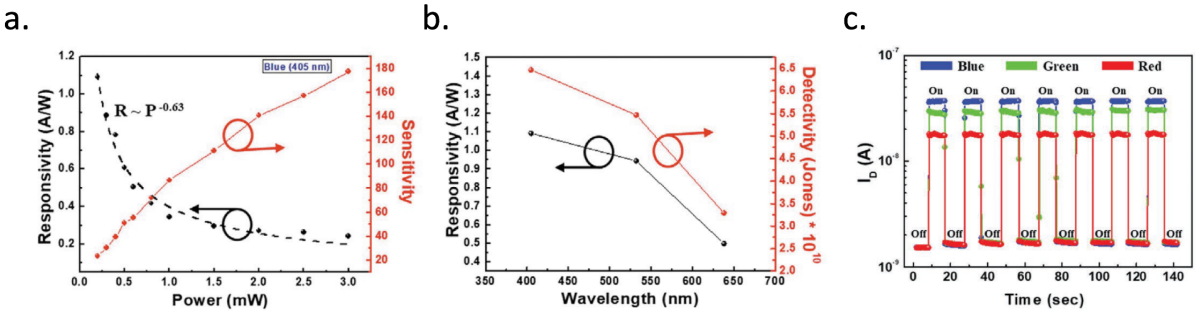

Figure 3.9: (a) The photoresponsivity and sensitivity measurements of the proposed photodiode under blue (405 nm) light illumination at different power ranges from $200\mu W$ to $3mW$. The photoresponsivity versus power intensity curve is fitted to the power law (RP_{inc}^{-1}). (b) The photoresponsivity and photodetectivity representations of various light illuminations with different wavelength (405, 532, and 638 nm) at same power of 500. (c) The photo-switching characteristics of the device under blue, green and red light illumination in 10 s pulses, up to 150 s at the same power of $200\mu W$. Adapted from Ref [30].

Next, the time-domain behaviour of the device was characterized by measuring its phororesponse under pulses of light with different wavelengths (638, 532, and 405 nm) at a constant $V_D = 1$ V. Under red light (638 nm) of intensity 200, the current increased by one order of magnitude with a rise time of 194.19ms and a fall time of 48.53ms. Green (blue) pulses of the same intensity generated larger increases in current (1.5 orders of magnitude) with rise time of 234.31 ms (127.14 ms) and fall time of 24.29 ms (127.12 ms), which can be seen in Fig.3.9(c). Also pictured is the

reproducibility of the photoresponse for seven cycles (repeats of 10s ON and 10 s OFF, with 150 s in total). Both the photoresponse amplitude and switching speed were stable throughout the measurement, demonstrating robustness.

In Fig.3.10 we compare this grounded-gate photodiode with recently reported PN homo/ heterojunctions using the benchmark parameters of device configuration, deposition method, responsivity, detectivity, and rise and fall times. In comparison to the other reported devices, the photodiode presented in this work demonstrates reliable photoresponsivity ($> 1AW^{-1}$), high photodetectivity (6×10^{10} Jones), and highly stable response time (100–200ms), which can be achieved through simple processing methods. The demonstrated grounded-gate MoS_2 photodiode therefore shows promising potential for next-generation applications in the field of optoelectronics.

Device Configuration	**Method**	**Responsivity (AW^{-1})**	**Detectivity (D*/jones)**	**Rise time**	**Fall time**	**Reference**
MoS_2 based Ground gated photodiode	Mechanical Exfoliation	~ 1.031	~ 6×10^{10}	~ 127.14 ms (λ = 405 nm) ~ 234.31 ms (λ = 532 nm) ~ 194.19 ms (λ = 638 nm)	~127.12 ms (λ = 405 nm) ~ 24.29 ms (λ = 532 nm) ~ 48.53 ms (λ = 638 nm)	This Work
MoS_2/Black Phosphorous (Heterojunction)	Mechanical Exfoliation	~ 0.153 (λ = 1.3 μm)	~ 2.13×10^9 (λ = 1550 nm)	15 μs	70 μs	[6]
MoS_2/Hbn/AuCl3 (Chemical dopant) (Homojunction)	Mechanical Exfoliation	~ 0.33 (reverse)	~ 1.6×10^{10}	100 – 200 ms	100 – 200 ms	[12]
WSe_2 (Homojunction)	Mechanical Exfoliation (Electrostatic gating)	~ 0.0007	NA	12.3 ± 0.2 ms	11.4 ± 0.2 ms.	[14]
MoS_2/Si (Heterojunction)	Magnetron Sputter	~ 0.3	~10^{13}	3 μs	40 μs	[20]
MoS_2/GaAs	CVD grown	~ 0.419	~ 1.9×10^{14}	6 s	3 s	[22]

Figure 3.10: Responsivity, detectivity and response time comparison of our MoS_2-based grounded-gate photodiode with recently reported PN junction photodetectors distinguished by device configuration. Adapted from Ref [30].

4

Strain-Tuning $PtSe_2$ for High ON-Current Lateral Tunnel Field-Effect Transistors

***Statement of Contributions**: I am the sole author of the contents of this chapter, which is under review at the time of submission of this thesis. This project was supervised by Prof. Youngki Yoon.*

4.1 Introduction

As energy dissipation becomes an increasingly pressing issue for modern electronics, the emergence of steep-switching devices poses low-power alternatives to conventional silicon transistors. One such device is the tunnel field-effect transistor (TFET), [57] in which current is driven by band-to-band tunneling rather than thermionic emission. This device is not subject to the fundamental thermionic switching limit of 60 mV/dec at 300 K, and presents an opportunity to operate at a low supply voltage and minimal leakage currents.

The operation of a TFET is briefly presented in Fig.4.1. The device consists of source, channel, drain, and gate terminals much like a conventional transistor. However, unlike in a MOSFET, in a TFET the source and drain are oppositely doped. When a drain voltage is applied, the band-bending in the channel region allows for two tunneling barriers to emerge at the source-channel and channel-drain junctions. Current can flow from the source to the drain when carriers

tunnel from the valence bands of the source to the conduction bands of the channel or drain. By controlling this band-bending, the gate bias can modulate the flow of tunneling current through these junctions. Going from the OFF state (where the channel bandgap is positioned such that it maximizes the thickness of the junction tunneling barriers) to the ON state (where a high gate bias causes one tunneling barrier to become significantly narrower) can be done very abruptly since the carriers being transported are taken from the heavily-populated valence band rather than the tail end of a fermi distribution in the conduction band. This leads to incredibly sharp switching characteristics, and subthreshold swings below 60 mV/dec.

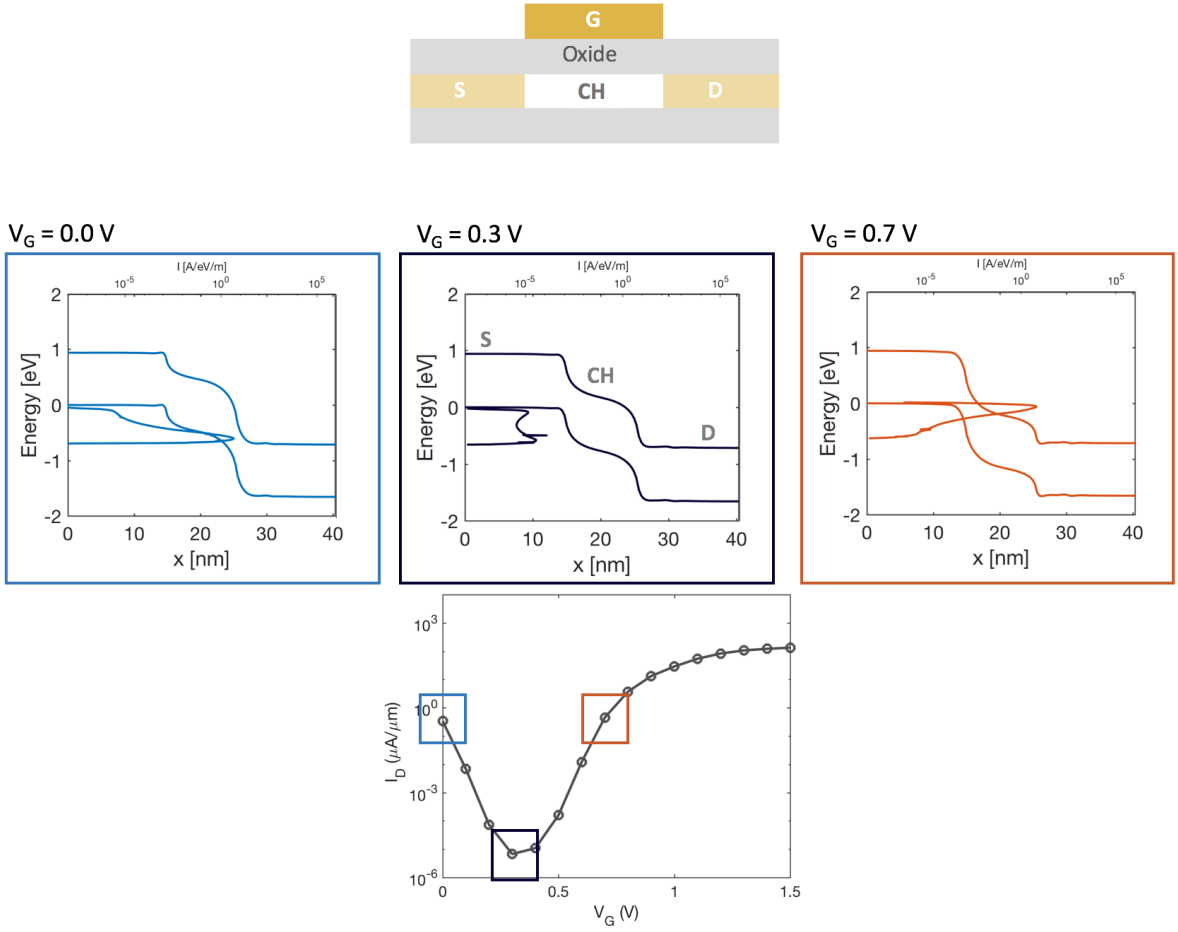

Figure 4.1: Operating mechanism of a TFET structure (top), showing the channel potential and current (middle row) and current-voltage characteristics (bottom) for the device in the ambipolar ON states (blue and red) and OFF state (black).

Achieving this sharp switching in practice requires excellent electrostatic control over the tunneling region, which has led to several investigations into using planar two-dimensional semiconductors such as phosphorene and the transition metal dichalcogenides (TMDs) as TFET channel materials [58, 59, 60, 7, 6, 61, 62]. These materials are atomically thin, which facilitates precise control over the tunnel barrier by a gate electrode. However, while the operating principles of a TFET allow for low OFF currents and steep switching characteristics, the ON-state performance is limited by material properties of the channel. The ON currents (I_{ON}) achievable with lateral TFET structures made from most well-studied monolayer TMDs are generally low due to their large bandgaps and large effective masses. [58] To boost the ON current while using two-dimensional channel materials, TFETs made with multilayer structures [59, 63] or vertical heterostructures [60, 64] have been proposed. However, these strategies may require more complex fabrication processes, and sacrifice the superior electrostatic control possible with an atomically thin monolayer.

It would be useful to instead overcome the shortfalls of 2D monolayer channels by employing methods to tune the relevant material parameters. Given the considerable flexibility of 2D monolayers, [65] mechanical strain is one such method. These materials have been strained using pressure differences [66], thermal expansion on flexible substrates [67], and applied electric fields [68], and the resulting modulations of material properties are in good agreement with theoretical predictions [66, 67, 68]. Strain-engineering therefore presents an opportunity to optimize the performance of monolayer TMD TFETs while using simple lateral architectures which makes full use of their thinness.

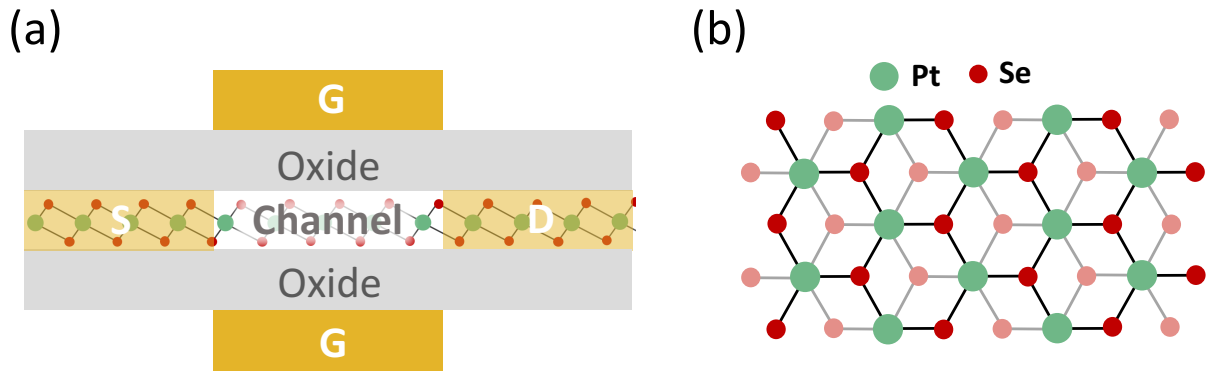

Figure 4.2: (a) A schematic of the double-gated lateral TFET structure simulated in this work, where the channel is made of monolayer $PtSe_2$ in the 1T phase. (b) Top view of the atomistic configuration of 1T-$PtSe_2$. The side-view is shown within the channel in (a).

In this chapter, we identify that strained monolayer platinum diselenide ($PtSe_2$) TFET devices can deliver high I_{ON} while maintaining steep switching characteristics. $PtSe_2$ is a newer addition

to the TMD family and the recent development of a direct-selenization monolayer growth method [69] has led to it being experimentally accessible for electronic applications. [70, 71, 72] We study the performance of strained $PtSe_2$ TFET devices using full-band quantum transport simulations to accurately capture carrier transport through satellite valleys which undergo changes in relative position under strain.

4.2 Channel Material Properties

The type of device structure considered here is a double-gated FET, as shown schematically in Fig. 4.2(a), and the channel material is monolayer $PtSe_2$ in its stable 1T phase (Fig. 4.2(b)). To first study how the channel material properties can be tuned by tensile strain, we construct a Hamiltonian matrix with tight-binding-like parameters for $PtSe_2$, using a basis of maximally localized Wannier functions (MLWF), which match density functional theory (DFT) bands. [73] DFT calculations are performed with Quantum Espresso, [25] within the generalized gradient approximation (GGA) with projector augmented wave (PAW) pseudopotentials. After an initial relaxation of the unit cell, biaxial tensile strain is implemented by changing its in-plane lattice dimensions according to $a_\epsilon = a_0(1+\epsilon)$, where ϵ is the strain considered, and a_0 and a_ϵ are the unstrained and strained lattice constants, respectively. This is followed by a fixed-cell relaxation of the atomic positions. We use an effective isotropic model [28] to extract dielectric constants (κ_{ch} = 20.35, 22.51, 26.25) and monolayer thickness (t_{ch} = 0.52 nm, 0.5 nm, 0.48 nm) for the strained cells (ϵ = 0%, 2.5%, 5%). Wannier90 is then used to extract tight-binding-like parameters using MLWF. [27] The calculated bandgap (1.34 eV) is slightly larger than the value experimentally determined (1.2 eV), [69] but this would not significantly change our conclusion.

Figure 4.3(b) shows a polar plot of effective masses for $PtSe_2$ subjected to 0%-5% biaxial tensile strain, where 0^o is along the $\Gamma \rightarrow M$ direction as indicated in Fig. 4.3(a). The conduction band minimum and valence band maximum at which the effective masses are calculated are labelled as 'A' and 'B', respectively. The smallest electron effective mass can be found at 180^o along the $M \rightarrow \Gamma$ direction, which decreases from $0.21m_0$ for unstrained $PtSe_2$ to $0.18m_0$ for 5% strained $PtSe_2$. The right panel of Fig. 4.3(c) presents the strain-induced change in bandstructure along the $\Gamma \rightarrow M$ direction. Under tensile strain, the maximum valence band energy along this path shifts from the Γ point to lie near the conduction band minimum along $\Gamma \rightarrow M$ (point 'A' in Fig. 4.3(a)). The left panel of Fig. 4.3(c) shows the imaginary wavevector solutions, which correspond to the rate of spatially-decaying eigenstates of the MLWF Hamiltonian. The states found within the gap are available for carriers to occupy during band-to-band tunneling. Although the valence band maximum lies along $\Gamma \rightarrow K$ (point 'B' in Fig. 4.3(a)), the existence of a smooth imaginary band connecting the direct gap at $\Gamma \rightarrow M$ (Fig. 4.3(c), left panel) implies that it would be the dominant path for tunneling current when the device is in the ON state. [74].

The strain-tuned bandgaps and reduced effective masses are benchmarked against those of similar

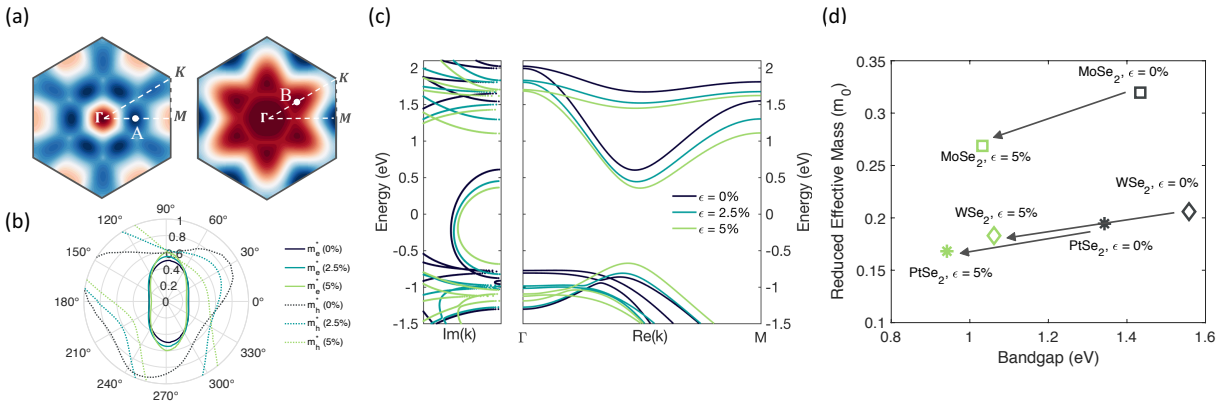

Figure 4.3: (a) Surface plot of the conduction band edge (left) and valence band edge (right) within the first Brillouin zone for $PtSe_2$ at $\epsilon = 0\%$. (b) Polar plot of the electron and hole effective masses (m_e^* and m_h^*). 0^o is equivalent to the $\Gamma \rightarrow M$ direction (the transport direction in this work). (c) Bandstructures for the strained $PtSe_2$ unit cells ($\epsilon = 0\%$, 2.5%, 5%) along the $\Gamma \rightarrow M$ direction, showing the real (right) and imaginary (left) values of the wavevector calculated using an extracted MLWF Hamiltonian. (d) Reduced effective mass (m_r^*) and bandgap for $PtSe_2$ at biaxial strains of $\epsilon = 0\%$ (black) and 5% (green), compared to similar monolayer XSe_2 materials.

moderate-gap XSe_2 materials in Fig. 4.3(d). We consider the $\Gamma \rightarrow K$ direction for $MoSe_2$ and WSe_2 since their smallest direct bandgaps lie at the K point. Under $\epsilon = 5\%$, $PtSe_2$ shows a bandgap of 0.94 eV and reduced effective mass of $0.17m_0$, lower than those of either $MoSe_2$ or WSe_2 under similar strain. Among the TMDs which have been experimentally grown in monolayer thus far, we have therefore identified $PtSe_2$ as one of the most promising candidates for strain-tuned tunneling enhancement.

4.3 Device Simulation Results

The ON-current in a lateral TFET can be expressed as

$$I_{ON} \propto exp\left(\frac{-\pi\Lambda\sqrt{m_r^* E_g}}{2\hbar(1+\Delta)}\right) \tag{4.1}$$

where Λ is the band-bending distance at the source-channel junction, m_r^* is the reduced effective mass ($1/m_r^* = 1/m_e^* + 1/m_h^*$), E_g is the bandgap, $\Delta = q(V_{DD} - V_{th})/E_g$ is the overdrive ratio, V_{DD} is the power supply voltage, and V_{th} is the threshold voltage. [75] The I_{ON} is inversely related to $\eta = \sqrt{m_r^* E_g}$, a quantity which can be significantly tuned by strain. To numerically

assess a device's ON-state characteristics resulting from the change in η when $PtSe_2$ is strained, we simulate three lateral TFET devices using channel materials of 0%, 2.5%, and 5% strained $PtSe_2$, respectively. The devices have channel lengths (L_{ch}) of 15 nm, source/drain extension lengths ($L_{S/D}$) of 15 nm, and 3.2 nm thick HfO_2 oxide layers (equivalent oxide thickness, EOT = 0.5 nm). Current is then calculated through the non-equilibrium Green's function transport framework, which is self-consistently solved with the Poisson equation. [76] Ballistic transport is assumed due to the relatively small device length considered. The V_{DD} is varied between 0.4 V and 0.8 V. The OFF current (I_{OFF}) is set to 1×10^{-5} $\mu A/\mu m$ (for drain voltage V_D = 0.4), 1×10^{-6} $\mu A/\mu m$ (for V_D = 0.6), and 1×10^{-7} $\mu A/\mu m$ (for V_D = 0.8) to ensure the device is in the ON state at V_G - V_{OFF} = V_D.

Figure 4.4(a) plots the I_D-V_G curves for the three devices. We start with a moderate V_D of 0.6 V and source (p-type)/drain(n-type) doping concentration ($N_{S/D}$) of $5.59\times10^{13}cm^{-2}$. The device with a 5% strained $PtSe_2$ channel has an I_{ON} (11.2 $\mu A/\mu m$) over two orders of magnitude higher than that of the unstrained channel (0.1 $\mu A/\mu m$), and a transconductance ($g_m = dI_D/dV_G$) over 100 times greater (87.12 $\mu S/\mu m$ vs. 0.78 $\mu S/\mu m$). We investigate the physical origin of these changes in Fig. 4.4(b), which shows the channel potential corresponding to I_{ON} for the devices in Fig. 4.4(a). In the ON state, the current is affected by the width of the source-channel tunneling barrier, which is quantified within the inset of Fig. 4.4(b). This tunneling barrier width decreases significantly with strain due to the reduced bandgap. The reduced effective mass would additionally allow for greater penetration of carrier wavefunctions through this thinner tunneling barrier. Since I_{ON} is highly dependent on V_D and $N_{S/D}$, we show heatmaps of I_{ON} for a range of these parameters in Fig. 4.5. The 5% strained $PtSe_2$ channel can achieve an I_{ON} of 116.2 $\mu A/\mu m$ at a V_D of 0.8 V and $N_{S/D}$ of $8.64\times10^{13}cm^{-2}$. We note that in our device with doped contacts, increasing $N_{S/D}$ narrows the depletion width, hence decreasing Λ in Eqn. (4.1) which boosts I_{ON}.

Next, we investigate the effects of strain on the OFF state characteristics. The minimum current in the OFF state (I_{min}) occurs when all transmission happens via direct leakage through the entire channel. In this case: [75]

$$I_{min} \propto exp(-2Im(k)L') \tag{4.2}$$

where L' is the 'effective channel length' which includes the channel length as well as the depletion width, and Im(k) is the imaginary value of the wavevector. The reduction of this quantity with strain (as seen in Fig. 4.3(c)) leads to increased penetration of carrier wavefunctions through the bandgap of the channel, and therefore increased leakage. As shown in Fig. 4.6(a), I_{min} is over two orders of magnitude larger for the 5% strained $PtSe_2$ device at a given L_{ch} due to its lower Im(k). I_{min} also drastically increases as L_{ch} decreases (left axis) unlike I_{ON} (right axis). A lower Im(k) is required for high tunneling transmission in the ON state, but there is an accompanying tradeoff in the leakage current which should be considered when optimizing the level of strain applied to the channel.

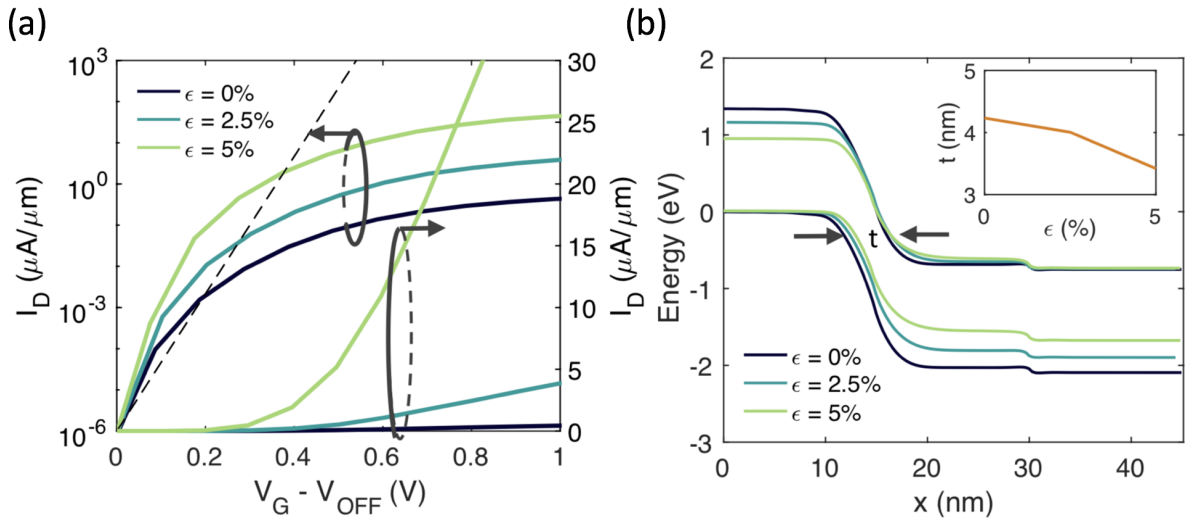

Figure 4.4: (a) I_D-V_G characteristics for the device shown in Fig. 4.2(a) for ϵ = 0%, 2.5%, and 5%, with the following nominal device parameters: L_{ch} = 15 nm, $L_{S/D}$ = 15 nm, $N_{S/D}$ = 5.59×10^{13}cm^{-2}, EOT = 0.5 nm and V_D = 0.6 V. (b) Potential profile along the device at V_G - V_{OFF} = 0.6 V for ϵ = 0%, 2.5%, and 5%. The inset quantifies the width of the tunneling barrier 't' as indicated in the main plot.

Finally, we examine the effects of strain on the minimum subthreshold swing (SS_{min}), which is influenced by the band bending at the tunneling barrier. In aggressively scaled devices, this band-bending is proportional to both the $N_{S/D}$ and the natural scaling length λ, which for a double-gated TFET structure is [77]:

$$\lambda = \sqrt{\frac{\kappa_{ch}}{2\kappa_{ox}}(1+\frac{\kappa_{ox}t_{ch}}{4\kappa_{ch}t_{ox}})t_{ch}t_{ox}} \tag{4.3}$$

Here, κ_{ch} is the channel permittivity, κ_{ox} is the oxide permittivity, and t_{ch} and t_{ox} are the channel and oxide thicknesses, respectively. A short natural scaling length indicates a sharper drop of electrostatic potential across the source-channel junction, which allows for the most abrupt opening of an energy window for tunneling into the conduction band of the channel, resulting in a low subthreshold swing. 2D monolayer channels benefit from smaller λ due to an atomically thin t_{ch}, leading to a lower SS in lateral TFETs compared to multilayer or bulk-material channels. The increase in κ_{ch} with biaxial tensile strain is compensated by a further decrease in t_{ch}, leading to an overall minimal increase in λ (1.19 nm for ϵ = 0% to 1.29 nm for ϵ = 5%). Figure 4.6(b) plots SS_{min} for the three devices considered as a function of channel length. The strained devices

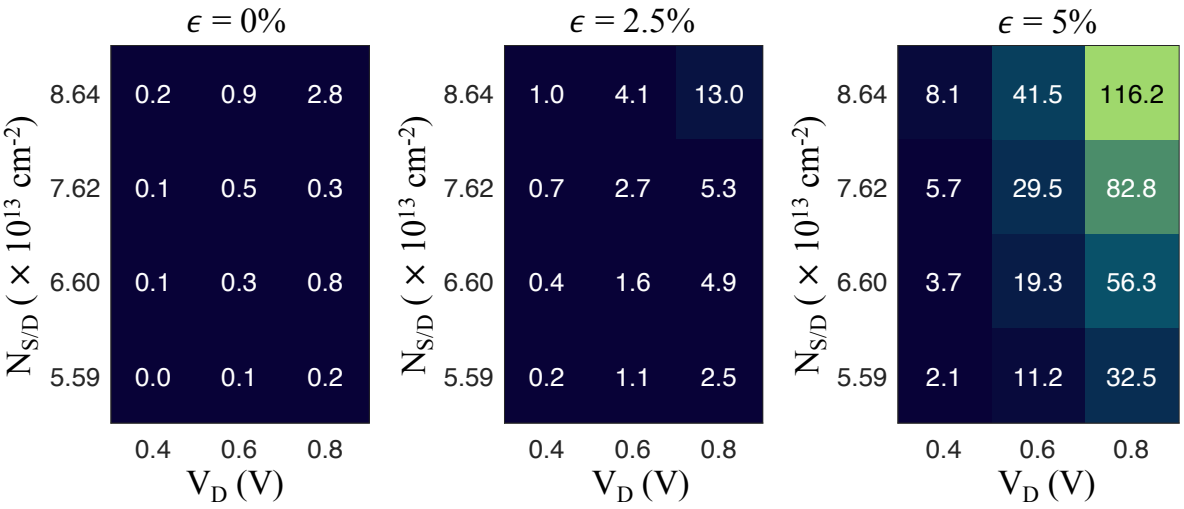

Figure 4.5: Heatmaps of I_{ON} (in $\mu A/\mu m$) at V_D = 0.4 V, 0.6 V, and 0.8 V, and $N_{S/D}$ = 5.59×10^{13}cm^{-2}, 6.60×10^{13}cm^{-2}, 7.62×10^{13}cm^{-2}, and 8.64×10^{13}cm^{-2} are shown for ϵ = 0% (left), 2.5% (middle), and 5% (right). I_{OFF} = 1×10^{-5} $\mu A/\mu m$, 1×10^{-6} $\mu A/\mu m$, and 1×10^{-7} $\mu A/\mu m$ were used for V_D = 0.4 V, 0.6 V, and 0.8 V, respectively.

maintain similar SS_{min} as the unstrained device for channel lengths down to 10 nm, showing that the scalability is not signficantly affected by the addition of strain until that point. We note that at very short channel lengths (L_{ch} < 10 nm), the SS_{min} is over 60 mV/dec since the direct leakage current through the channel engulfs the entire subthreshold region.

4.4 Conclusion

In summary, strained-$PtSe_2$ TFETs benefit from high electrostatic control with an atomically thin monolayer, while also being able to deliver high ON currents due to the emergence of a smaller direct gap and a lighter effective mass. A double-gated $PtSe_2$ device under 5% biaxial tensile strain can reach an I_{ON} above 116 $\mu A/\mu m$ at a V_D of 0.8 V, while maintaining an I_{OFF} below 1×10^{-7} $\mu A/\mu m$ and SS well under 60 mV/dec. This device can be scaled down to 10 nm before encountering performance degradation. Our work holds relevance for the emerging field of 2D-straintronics, and reveals that the potential of 2D monolayers for TFET applications cannot be dismissed.

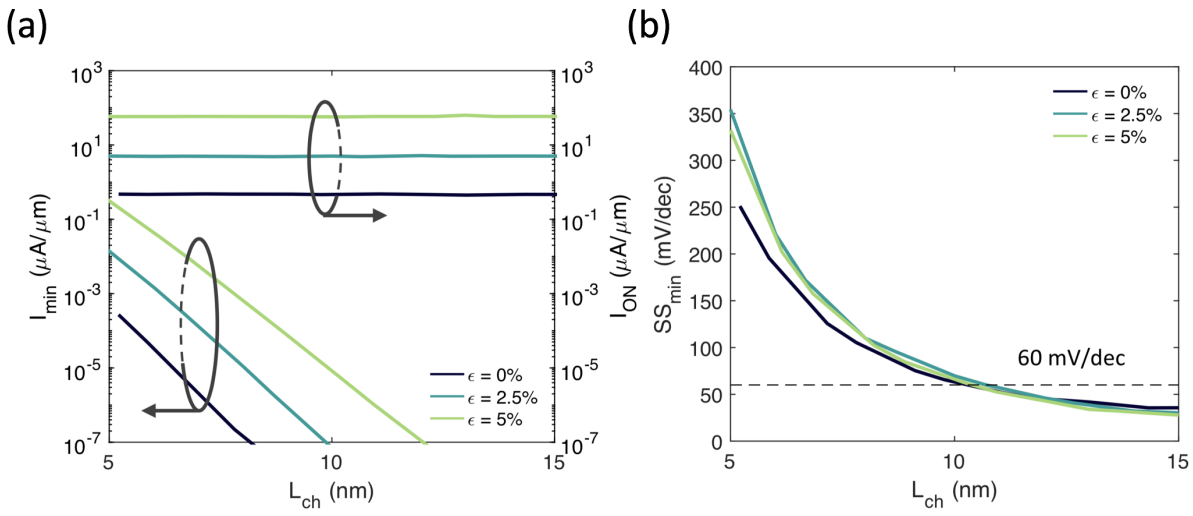

Figure 4.6: (a) Minimum leakage current (I_{min}, left axis) and I_{ON} (right axis) and (b) minimum subthreshold swing (SS_{min}) as a function of L_{ch} for the devices using ϵ = 0%, 2.5%, and 5% strained $PtSe_2$ channel, with $N_{S/D} = 5.59\times10^{13}cm^{-2}$ and V_D = 0.6 V.

5

Conclusions

In this thesis, ab-initio simulations were used to demonstrate the potential of 2D transition metal dichalcogenides for optoelectronic devices. In chapter 3, we developed a novel grounded-gate photodetector design, which harnessed the superior electrostatic-control achievable with an atomically-thin MoS_2 channel to achieve rectifying characteristics in a two-terminal device and minimize dark current. The resulting device therefore shows a high sensitivity to light, indicating its potential for photodetector applications. In chapter 4, mechanical strain was used to tune material parameters of 2D $PtSe_2$ to demonstrate a TFET with high ON-current. Since TMDs are highly flexible, mechanical strain - which can be implemented during the fabrication process, or through physical bending - is able to tune properties such as the bandgap and effective mass in a large range. The addition of strain is proposed as a simpler alternative to more experimentally-involved strategies since it is capable of improving performance without sacrificing the steep switching and improved scalability of an atomically-thin device channel.

5.1 Future Work

Although the work in Chapter 4 uses PtS_2 due to its relative experimental maturity, there are numerous other 2D monolayer materials not yet experimentally realized which could show even better tunability under strain. For example, SnTe, TiNBr, and TiNCl [60] all have I_{ON} above 100 $\mu A/\mu m$ in simulated monolayer TFETs, which is orders of magnitude higher than that of most transition metal dichalcogenides. Architectural optimizations, such as using a heterogate dielectric to reduce ambipolar transport characteristics, could also be explored as a way to minimize leakage currents in conjunction with increased I_{ON}. Other physical effects, such as spin-orbit coupling, could also be included in future works to see if they would improve or hinder performance in reality. It would also be interesting to explore uniaxial or shear strains to see if symmetry-breaking effects could be harnessed for improved device performance.

In terms of computational work, possible next steps would be to investigate scattering-assisted processes and how they would affect the current when modelling these transistor devices. Although we operate well within the ballistic limit of transport at the length scales considered, scattering from impurities (due to doping, for example) may still affect the results. Being able to model experimental realities would allow device physicists to go beyond the ideal case when assessing new materials. It would also be relevant to extend this work past simpler planar architectures and consider 3D FinFET structures, which may deliver the ultimate level of electrostatic control when used with atomically thin 2D materials.

Beyond the scope of this thesis, much of the future work towards realizing 2D material devices is on the experimental side. 2D materials are becoming increasingly promising for inclusion into a standard electronics fabrication process, but they are still in the nascent stages of development compared to conventional materials such as silicon and gallium arsenide. Bringing them to experimental maturity is currently an active field of study as methods are being developed to grow these materials in large-area [78], dope them [79], and improve contact properties [80].

5.2 Statement of Contributions

The following articles were submitted/published during the course of this degree, and my individual contributions are indicated. This text is also included under the title of each chapter.

- Chapter 3: The work in this chapter is adapted from the journal article "Ultrasensitive Multilayer MoS_2-Based Photodetector with Permanently Grounded Gate Effect", which was published in *Advanced Electronic Materials* in Febuary 2020 [30]. As an equal-contributing author, I preformed all of the simulations within this paper, prepared figures 1a-b, 2b-d, 3a-b, and 6a-b, and wrote the corresponding sections, assisted by Richard Han from the University of Waterloo. The device fabrication and collection of all experimental data was done by Mohammed Naqi, Sooho Choo, Sangjin Kang, and Jeonghun Kim from Sungkyunkwan University. The project was supervised by Prof. Youngki Yoon (University of Waterloo) and Prof. Sunkook Kim (Sungkyunkwan University).
- Chapter 4: I am the sole author of the contents of this chapter. A slightly modified version of this chapter has been submitted for publication at the time of submission of this thesis, and is under review. This project was supervised by Prof. Youngki Yoon.

The following article was written during the course of this degree, but is not included within this thesis:

- "Photoresponse of $MoSe_2$ Transistors : A Fully Numerical Quantum Transport Simulation Study", published in *ACS Applied Electronic Materials* in October 2020, authored by Gyuchull Han, Manasa Kaniselvan, and Youngki Yoon [81].

References

[1] K. S. Novoselov, "Electric field effect in atomically thin carbon films," *Science*, vol. 306, pp. 666–669, oct 2004.

[2] N. Mounet, M. Gibertini, P. Schwaller, D. Campi, A. Merkys, A. Marrazzo, T. Sohier, I. E. Castelli, A. Cepellotti, G. Pizzi, and N. Marzari, "Two-dimensional materials from high-throughput computational exfoliation of experimentally known compounds," *Nature Nanotechnology*, vol. 13, pp. 246–252, feb 2018.

[3] D. Akinwande, N. Petrone, and J. Hone, "Two-dimensional flexible nanoelectronics," *Nature Communications*, vol. 5, dec 2014.

[4] D. Akinwande, C. Huyghebaert, C.-H. Wang, M. I. Serna, S. Goossens, L.-J. Li, H.-S. P. Wong, and F. H. L. Koppens, "Graphene and two-dimensional materials for silicon technology," *Nature*, vol. 573, pp. 507–518, sep 2019.

[5] Y. Liu, X. Duan, H.-J. Shin, S. Park, Y. Huang, and X. Duan, "Promises and prospects of two-dimensional transistors," *Nature*, vol. 591, pp. 43–53, mar 2021.

[6] X. Jiang, X. Shi, M. Zhang, Y. Wang, Z. Gu, L. Chen, H. Zhu, K. Zhang, Q. Sun, and D. W. Zhang, "A symmetric tunnel field-effect transistor based on MoS_2/black phosphorus/MoS_2 nanolayered heterostructures," *ACS Applied Nano Materials*, vol. 2, pp. 5674–5680, jul 2019.

[7] D. Sarkar, X. Xie, W. Liu, W. Cao, J. Kang, Y. Gong, S. Kraemer, P. M. Ajayan, and K. Banerjee, "A subthermionic tunnel field-effect transistor with an atomically thin channel," *Nature*, vol. 526, pp. 91–95, sep 2015.

[8] N. Oliva, J. Backman, L. Capua, M. Cavalieri, M. Luisier, and A. M. Ionescu, "WSe_2/$SnSe_2$ vdW heterojunction tunnel FET with subthermionic characteristic and MOSFET co-integrated on same WSe_2 flake," *npj 2D Materials and Applications*, vol. 4, apr 2020.

[9] Y. Balaji, Q. Smets, Á. Szabo, M. Mascaro, D. Lin, I. Asselberghs, I. Radu, M. Luisier, and G. Groeseneken, "MoS_2/$MoTe_2$ heterostructure tunnel FETs using gated schottky contacts," *Advanced Functional Materials*, vol. 30, p. 1905970, nov 2019.

[10] J. Jiang, K. Parto, W. Cao, and K. Banerjee, "Ultimate monolithic-3D integration with 2D materials: Rationale, prospects, and challenges," *IEEE Journal of the Electron Devices Society*, vol. 7, pp. 878–887, 2019.

[11] M. Bernardi, M. Palummo, and J. C. Grossman, "Extraordinary sunlight absorption and one nanometer thick photovoltaics using two-dimensional monolayer materials," *Nano Letters*, vol. 13, pp. 3664–3670, jul 2013.

[12] S. Gupta, S. N. Shirodkar, A. Kutana, and B. I. Yakobson, "In pursuit of 2D materials for maximum optical response," *ACS Nano*, vol. 12, pp. 10880–10889, sep 2018.

[13] G. Konstantatos, "Current status and technological prospect of photodetectors based on two-dimensional materials," *Nature Communications*, vol. 9, dec 2018.

[14] D. D. Fazio, I. Goykhman, D. Yoon, M. Bruna, A. Eiden, S. Milana, U. Sassi, M. Barbone, D. Dumcenco, K. Marinov, A. Kis, and A. C. Ferrari, "High responsivity, large-area graphene/MoS_2 flexible photodetectors," *ACS Nano*, vol. 10, pp. 8252–8262, sep 2016.

[15] K. Ye, L. Liu, Y. Liu, A. Nie, K. Zhai, J. Xiang, B. Wang, F. Wen, C. Mu, Z. Zhao, Y. Gong, Z. Liu, and Y. Tian, "Lateral bilayer MoS_2–WS_2 heterostructure photodetectors with high responsivity and detectivity," *Advanced Optical Materials*, vol. 7, p. 1900815, jul 2019.

[16] H. Xu, J. Wu, Q. Feng, N. Mao, C. Wang, and J. Zhang, "High responsivity and gate tunable graphene-MoS_2 hybrid phototransistor," *Small*, vol. 10, pp. 2300–2306, mar 2014.

[17] N. Li, Q. Wang, C. Shen, Z. Wei, H. Yu, J. Zhao, X. Lu, G. Wang, C. He, L. Xie, J. Zhu, L. Du, R. Yang, D. Shi, and G. Zhang, "Large-scale flexible and transparent electronics based on monolayer molybdenum disulfide field-effect transistors," *Nature Electronics*, vol. 3, pp. 711–717, sep 2020.

[18] S. Bertolazzi, J. Brivio, and A. Kis, "Stretching and breaking of ultrathin MoS_2," *ACS Nano*, vol. 5, pp. 9703–9709, nov 2011.

[19] H. Peelaers and C. G. V. de Walle, "Effects of strain on band structure and effective masses in MoS_2," *Physical Review B*, vol. 86, dec 2012.

[20] C. Klinkert, Á. Szabó, C. Stieger, D. Campi, N. Marzari, and M. Luisier, "2-d materials for ultrascaled field-effect transistors: One hundred candidates under the ab initio microscope," *ACS Nano*, vol. 14, pp. 8605–8615, jun 2020.

[21] E. G. Marin, M. Perucchini, D. Marian, G. Iannaccone, and G. Fiori, "Modeling of electron devices based on 2-d materials," *IEEE Transactions on Electron Devices*, vol. 65, pp. 4167–4179, oct 2018.

[22] T. Kato, "On the eigenfunctions of many-particle systems in quantum mechanics," *Communications on Pure and Applied Mathematics*, vol. 10, no. 2, pp. 151–177, 1957.

[23] W. Kohn and L. J. Sham, "Self-consistent equations including exchange and correlation effects," *Physical Review*, vol. 140, pp. A1133–A1138, nov 1965.

[24] J. P. Perdew, J. A. Chevary, S. H. Vosko, K. A. Jackson, M. R. Pederson, D. J. Singh, and C. Fiolhais, "Atoms, molecules, solids, and surfaces: Applications of the generalized gradient approximation for exchange and correlation," *Physical Review B*, vol. 46, pp. 6671–6687, sep 1992.

[25] P. Giannozzi, S. Baroni, N. Bonini, M. Calandra, R. Car, C. Cavazzoni, D. Ceresoli, G. L. Chiarotti, M. Cococcioni, I. Dabo, A. D. Corso, S. de Gironcoli, S. Fabris, G. Fratesi, R. Gebauer, U. Gerstmann, C. Gougoussis, A. Kokalj, M. Lazzeri, L. Martin-Samos, N. Marzari, F. Mauri, R. Mazzarello, S. Paolini, A. Pasquarello, L. Paulatto, C. Sbraccia, S. Scandolo, G. Sclauzero, A. P. Seitsonen, A. Smogunov, P. Umari, and R. M. Wentzcovitch, "QUANTUM ESPRESSO: a modular and open-source software project for quantum simulations of materials," *Journal of Physics: Condensed Matter*, vol. 21, p. 395502, sep 2009.

[26] N. Marzari, A. A. Mostofi, J. R. Yates, I. Souza, and D. Vanderbilt, "Maximally localized wannier functions: Theory and applications," *Reviews of Modern Physics*, vol. 84, pp. 1419–1475, oct 2012.

[27] A. A. Mostofi, J. R. Yates, G. Pizzi, Y.-S. Lee, I. Souza, D. Vanderbilt, and N. Marzari, "An updated version of wannier90: A tool for obtaining maximally-localised wannier functions," *Computer Physics Communications*, vol. 185, pp. 2309–2310, aug 2014.

[28] T. Sohier, M. Calandra, and F. Mauri, "Two-dimensional fröhlich interaction in transition-metal dichalcogenide monolayers: Theoretical modeling and first-principles calculations," *Physical Review B*, vol. 94, aug 2016. doi: 10.1103/physrevb.94.085415.

[29] A. Laturia, M. L. V. de Put, and W. G. Vandenberghe, "Dielectric properties of hexagonal boron nitride and transition metal dichalcogenides: from monolayer to bulk," *npj 2D Materials and Applications*, vol. 2, mar 2018.

[30] M. Naqi, M. Kaniselvan, S. Choo, G. Han, S. Kang, J. Kim, Y. Yoon, and S. Kim, "Ultrasensitive multilayer MoS_2-based photodetector with permanently grounded gate effect," *Advanced Electronic Materials*, vol. 6, p. 1901256, feb 2020.

[31] M. Bernardi, M. Palummo, and J. C. Grossman, "Extraordinary sunlight absorption and one nanometer thick photovoltaics using two-dimensional monolayer materials," *Nano Letters*, vol. 13, pp. 3664–3670, jul 2013.

[32] H. Lee, J. Ahn, S. Im, J. Kim, and W. Choi, "High-responsivity multilayer $MoSe_2$ phototransistors with fast response time," *Scientific Reports*, vol. 8, aug 2018.

[33] Z. Qi, T. Yang, D. Li, H. Li, X. Wang, X. Zhang, F. Li, W. Zheng, P. Fan, X. Zhuang, and A. Pan, "High-responsivity two-dimensional p-PbI_2/n-WS_2 vertical heterostructure photodetectors enhanced by photogating effect," *Materials Horizons*, vol. 6, no. 7, pp. 1474–1480, 2019.

[34] S. Kim, J. Maassen, J. Lee, S. M. Kim, G. Han, J. Kwon, S. Hong, J. Park, N. Liu, Y. C. Park, I. Omkaram, J.-S. Rhyee, Y. K. Hong, and Y. Yoon, "Interstitial mo-assisted photovoltaic effect in multilayer $MoSe_2$ phototransistors," *Advanced Materials*, vol. 30, p. 1705542, jan 2018.

[35] H. Wang, C. Zhang, W. Chan, S. Tiwari, and F. Rana, "Ultrafast response of monolayer molybdenum disulfide photodetectors," *Nature Communications*, vol. 6, nov 2015.

[36] W. Choi, M. Y. Cho, A. Konar, J. H. Lee, G.-B. Cha, S. C. Hong, S. Kim, J. Kim, D. Jena, J. Joo, and S. Kim, "Phototransistors: High-detectivity multilayer MoS_2 phototransistors with spectral response from ultraviolet to infrared (adv. mater. 43/2012)," *Advanced Materials*, vol. 24, pp. 5902–5902, nov 2012.

[37] C. Xie, C. Mak, X. Tao, and F. Yan, "Photodetectors based on two-dimensional layered materials beyond graphene," *Advanced Functional Materials*, vol. 27, p. 1603886, nov 2016.

[38] M. S. Choi, D. Qu, D. Lee, X. Liu, K. Watanabe, T. Taniguchi, and W. J. Yoo, "Lateral MoS_2 p–n junction formed by chemical doping for use in high-performance optoelectronics," *ACS Nano*, vol. 8, pp. 9332–9340, aug 2014.

[39] S. Wi, H. Kim, M. Chen, H. Nam, L. J. Guo, E. Meyhofer, and X. Liang, "Enhancement of photovoltaic response in multilayer MoS_2 induced by plasma doping," *ACS Nano*, vol. 8, pp. 5270–5281, may 2014.

[40] Y. Jin, D. H. Keum, S.-J. An, J. Kim, H. S. Lee, and Y. H. Lee, "A van der waals homojunction: Ideal p-n diode behavior in $MoSe_2$," *Advanced Materials*, vol. 27, pp. 5534–5540, aug 2015.

[41] D. J. Groenendijk, M. Buscema, G. A. Steele, S. M. de Vasconcellos, R. Bratschitsch, H. S. J. van der Zant, and A. Castellanos-Gomez, "Photovoltaic and photothermoelectric effect in a double-gated WSe_2 device," *Nano Letters*, vol. 14, pp. 5846–5852, sep 2014.

[42] L. Wang, J. Jie, Z. Shao, Q. Zhang, X. Zhang, Y. Wang, Z. Sun, and S.-T. Lee, "MoS_2/si heterojunction with vertically standing layered structure for ultrafast, high-detectivity, self-driven visible-near infrared photodetectors," *Advanced Functional Materials*, vol. 25, pp. 2910–2919, mar 2015.

[43] O. Lopez-Sanchez, E. A. Llado, V. Koman, A. F. i Morral, A. Radenovic, and A. Kis, "Light generation and harvesting in a van der waals heterostructure," *ACS Nano*, vol. 8, pp. 3042–3048, mar 2014.

[44] Z. Xu, S. Lin, X. Li, S. Zhang, Z. Wu, W. Xu, Y. Lu, and S. Xu, "Monolayer MoS_2 /GaAs heterostructure self-driven photodetector with extremely high detectivity," *Nano Energy*, vol. 23, pp. 89–96, may 2016.

[45] J. Y. Kwak, J. Hwang, B. Calderon, H. Alsalman, N. Munoz, B. Schutter, and M. G. Spencer, "Electrical characteristics of multilayer MoS_2 FET's with MoS_2/graphene heterojunction contacts," *Nano Letters*, vol. 14, pp. 4511–4516, jul 2014.

[46] Z. Huang, W. Han, H. Tang, L. Ren, D. S. Chander, X. Qi, and H. Zhang, "Photoelectrochemical-type sunlight photodetector based on MoS_2/graphene heterostructure," *2D Materials*, vol. 2, p. 035011, jul 2015.

[47] L. Ye, H. Li, Z. Chen, and J. Xu, "Near-infrared photodetector based on MoS_2/black phosphorus heterojunction," *ACS Photonics*, vol. 3, pp. 692–699, mar 2016.

[48] Y. Deng, Z. Luo, N. J. Conrad, H. Liu, Y. Gong, S. Najmaei, P. M. Ajayan, J. Lou, X. Xu, and P. D. Ye, "Black phosphorus–monolayer MoS_2 van der waals heterojunction p–n diode," *ACS Nano*, vol. 8, pp. 8292–8299, jul 2014.

[49] Q. Ren, Q. Xu, H. Xia, X. Luo, F. Zhao, L. Sun, Y. Li, W. Lv, L. Du, Y. Peng, and Z. Zhao, "High performance photoresponsive field-effect transistors based on MoS_2/pentacene heterojunction," *Organic Electronics*, vol. 51, pp. 142–148, dec 2017.

[50] Y. Peng, R. Ding, Q. Ren, S. Xu, L. Sun, Y. Wang, and F. Lu, "High performance photodiode based on MoS_2/pentacene heterojunction," *Applied Surface Science*, vol. 459, pp. 179–184, nov 2018.

[51] M. Long, P. Wang, H. Fang, and W. Hu, "Progress, challenges, and opportunities for 2D material based photodetectors," *Advanced Functional Materials*, vol. 29, p. 1803807, sep 2018.

[52] N. Huo and G. Konstantatos, "Recent progress and future prospects of 2D-based photodetectors," *Advanced Materials*, vol. 30, p. 1801164, jul 2018.

[53] A. D. Bartolomeo, G. Luongo, F. Giubileo, N. Funicello, G. Niu, T. Schroeder, M. Lisker, and G. Lupina, "Hybrid graphene/silicon schottky photodiode with intrinsic gating effect," *2D Materials*, vol. 4, p. 025075, apr 2017.

[54] A. D. Bartolomeo, A. Grillo, F. Urban, L. Iemmo, F. Giubileo, G. Luongo, G. Amato, L. Croin, L. Sun, S.-J. Liang, and L. K. Ang, "Asymmetric schottky contacts in bilayer MoS_2 field effect transistors," *Advanced Functional Materials*, vol. 28, p. 1800657, may 2018.

[55] M. M. Furchi, D. K. Polyushkin, A. Pospischil, and T. Mueller, "Mechanisms of photoconductivity in atomically thin MoS_2," *Nano Letters*, vol. 14, pp. 6165–6170, oct 2014.

[56] J. Yu, B. J. Kim, S. Park, I. K. Han, and S. J. Kang, "Red/green/blue selective phototransistors with a hybrid structure of quantum-dots and an oxide semiconductor," *Japanese Journal of Applied Physics*, vol. 57, p. 044001, mar 2018.

[57] A. M. Ionescu and H. Riel, "Tunnel field-effect transistors as energy-efficient electronic switches," *Nature*, vol. 479, pp. 329–337, nov 2011. doi: 10.1038/nature10679.

[58] H. Ilatikhameneh, Y. Tan, B. Novakovic, G. Klimeck, R. Rahman, and J. Appenzeller, "Tunnel field-effect transistors in 2-d transition metal dichalcogenide materials," *IEEE Journal on Exploratory Solid-State Computational Devices and Circuits*, vol. 1, pp. 12–18, dec 2015. doi: 10.1109/jxcdc.2015.2423096.

[59] T. A. Ameen, H. Ilatikhameneh, G. Klimeck, and R. Rahman, "Few-layer phosphorene: An ideal 2D material for tunnel transistors," *Scientific Reports*, vol. 6, jun 2016. doi: 10.1038/srep28515.

[60] A. Szabo, C. Klinkert, D. Campi, C. Stieger, N. Marzari, and M. Luisier, "*Ab Initio* simulation of band-to-band tunneling FETs with single- and few-layer 2-d materials as channels," *IEEE Transactions on Electron Devices*, vol. 65, pp. 4180–4187, oct 2018. doi: 10.1109/ted.2018.2840436.

[61] P. K. Dubey and B. K. Kaushik, "A charge plasma-based monolayer transition metal dichalcogenide tunnel FET," *IEEE Transactions on Electron Devices*, vol. 66, pp. 2837–2843, jun 2019. doi: 10.1109/ted.2019.2909182.

[62] S. Das, A. Prakash, R. Salazar, and J. Appenzeller, "Toward low-power electronics: Tunneling phenomena in transition metal dichalcogenides," *ACS Nano*, vol. 8, pp. 1681–1689, jan 2014. doi: 10.1021/nn406603h.

[63] D. Yin and Y. Yoon, "Design strategy of two-dimensional material field-effect transistors: Engineering the number of layers in phosphorene FETs," *Journal of Applied Physics*, vol. 119, p. 214312, jun 2016. doi: 10.1063/1.4953256.

[64] A. Szabo, S. J. Koester, and M. Luisier, "Ab-initio simulation of van der waals $MoTe_2$–SnS_2 heterotunneling FETs for low-power electronics," *IEEE Electron Device Letters*, vol. 36, pp. 514–516, may 2015. doi: 10.1109/led.2015.2409212.

[65] A. Castellanos-Gomez, M. Poot, G. A. Steele, H. S. J. van der Zant, N. Agraït, and G. Rubio-Bollinger, "Elastic properties of freely suspended MoS_2 nanosheets," *Advanced Materials*, vol. 24, pp. 772–775, jan 2012. doi: 10.1002/adma.201103965.

[66] D. Lloyd, X. Liu, J. W. Christopher, L. Cantley, A. Wadehra, B. L. Kim, B. B. Goldberg, A. K. Swan, and J. S. Bunch, "Band gap engineering with ultralarge biaxial strains in suspended monolayer MoS_2," *Nano Letters*, vol. 16, pp. 5836–5841, aug 2016. doi: 10.1021/acs.nanolett.6b02615.

[67] R. Frisenda, M. Drüppel, R. Schmidt, S. M. de Vasconcellos, D. P. de Lara, R. Bratschitsch, M. Rohlfing, and A. Castellanos-Gomez, "Biaxial strain tuning of the optical properties of single-layer transition metal dichalcogenides," *npj 2D Materials and Applications*, vol. 1, may 2017. doi: 10.1038/s41699-017-0013-7.

[68] Z. Peng, X. Chen, Y. Fan, D. J. Srolovitz, and D. Lei, "Strain engineering of 2D semiconductors and graphene: from strain fields to band-structure tuning and photonic applications," *Light: Science & Applications*, vol. 9, nov 2020. doi: 10.1038/s41377-020-00421-5.

[69] Y. Wang, L. Li, W. Yao, S. Song, J. T. Sun, J. Pan, X. Ren, C. Li, E. Okunishi, Y.-Q. Wang, E. Wang, Y. Shao, Y. Y. Zhang, H. tao Yang, E. F. Schwier, H. Iwasawa, K. Shimada, M. Taniguchi, Z. Cheng, S. Zhou, S. Du, S. J. Pennycook, S. T. Pantelides, and H.-J. Gao, "Monolayer $PtSe_2$, a new semiconducting transition-metal-dichalcogenide, epitaxially grown by direct selenization of pt," *Nano Letters*, vol. 15, pp. 4013–4018, may 2015. doi: 10.1021/acs.nanolett.5b00964.

[70] R. A. B. Villaos, C. P. Crisostomo, Z.-Q. Huang, S.-M. Huang, A. A. B. Padama, M. A. Albao, H. Lin, and F.-C. Chuang, "Thickness dependent electronic properties of pt dichalcogenides," *npj 2D Materials and Applications*, vol. 3, jan 2019. doi: 10.1038/s41699-018-0085-z.

[71] T. Das, E. Yang, J. E. Seo, J. H. Kim, E. Park, M. Kim, D. Seo, J. Y. Kwak, and J. Chang, "Doping-free all $PtSe_2$ transistor via thickness-modulated phase transition," *ACS Applied Materials & Interfaces*, vol. 13, pp. 1861–1871, jan 2021. doi: 10.1021/acsami.0c17810.

[72] C. Yim, K. Lee, N. McEvoy, M. O'Brien, S. Riazimehr, N. C. Berner, C. P. Cullen, J. Kotakoski, J. C. Meyer, M. C. Lemme, and G. S. Duesberg, "High-performance hybrid electronic devices from layered $PtSe_2$ films grown at low temperature," *ACS Nano*, vol. 10, pp. 9550–9558, sep 2016. doi: 10.1021/acsnano.6b04898.

[73] A. AlMutairi, D. Yin, and Y. Yoon, "$PtSe_2$ field-effect transistors: New opportunities for electronic devices," *IEEE Electron Device Letters*, vol. 39, pp. 151–154, jan 2018. doi: 10.1109/led.2017.2773599.

[74] M. Luisier and G. Klimeck, "Simulation of nanowire tunneling transistors: From the wentzel–kramers–brillouin approximation to full-band phonon-assisted tunneling," *Journal of Applied Physics*, vol. 107, p. 084507, apr 2010. doi: 10.1063/1.3386521.

[75] H. Ilatikhameneh, R. B. Salazar, G. Klimeck, R. Rahman, and J. Appenzeller, "From fowler–nordheim to nonequilibrium green's function modeling of tunneling," *IEEE Transactions on Electron Devices*, vol. 63, pp. 2871–2878, jul 2016. doi: 10.1109/ted.2016.2565582.

[76] S. Datta, *Quantum Transport: Atom to Transistor*. Cambridge University Press, 2005. doi: 10.1017/cbo9781139164313.

[77] L. Liu, D. Mohata, and S. Datta, "Scaling length theory of double-gate interband tunnel field-effect transistors," *IEEE Transactions on Electron Devices*, vol. 59, pp. 902–908, apr 2012. doi: 10.1109/ted.2012.2183875.

[78] A. Quellmalz, X. Wang, S. Sawallich, B. Uzlu, M. Otto, S. Wagner, Z. Wang, M. Prechtl, O. Hartwig, S. Luo, G. S. Duesberg, M. C. Lemme, K. B. Gylfason, N. Roxhed, G. Stemme, and F. Niklaus, "Large-area integration of two-dimensional materials and their heterostructures by wafer bonding," *Nature Communications*, vol. 12, feb 2021.

[79] C. J. McClellan, E. Yalon, K. K. H. Smithe, S. V. Suryavanshi, and E. Pop, "High current density in monolayer MoS_2 doped by AlO_x," *ACS Nano*, vol. 15, pp. 1587–1596, jan 2021.

[80] D. G. Purdie, N. M. Pugno, T. Taniguchi, K. Watanabe, A. C. Ferrari, and A. Lombardo, "Cleaning interfaces in layered materials heterostructures," *Nature Communications*, vol. 9, dec 2018.

[81] G. Han, M. Kaniselvan, and Y. Yoon, "Photoresponse of $MoSe_2$ transistors: A fully numerical quantum transport simulation study," *ACS Applied Electronic Materials*, vol. 2, pp. 3765–3772, nov 2020.